J. Appl. Comput. Mech., xx(x) (2026) 1-20
DOI: 10.22055/jacm.2026.49487.6020

ISSN: 2383-4536
jacm.scu.ac.ir

Shahid Chamran University of Ahvaz

Journal of Applied and Computational Mechanics

Research Paper

Vortex Formation Evolution in Melting of Metal-Foam-Embedded Nano-Enhanced Phase Change Materials Regulated by Dual-Directional Helmholtz Coil Magnetic Fields

Zhuotao Li[1], Yijie Zhuang[1], Pan Jia[2]

[1] School of Environmental Science and Engineering, Guangdong University of Technology, Guangzhou, 510006, China
[2] School of Science, Harbin Institute of Technology, Shenzhen, 518055, China

Received June 21 2026; Revised September 20 2026; Accepted for publication September 20 2026.
✉ Corresponding authors: Y. Zhuang (zyj7933@gdut.edu.cn); P. Jia (jiapan@hit.edu.cn)

Abstract. A numerical study is conducted to investigate the regulation mechanism of dual-directional magnetic fields generated by Helmholtz coils on the vortex modes and melting performance of nano-enhanced phase change material (NEPCM) embedded in metal foam. The enthalpy-porosity method, Darcy-Forchheimer model and local thermal non-equilibrium model are used to describe the melting process, flow in porous media and heat transfer, respectively. The proposed model is then validated against experiments, then the effects of magnetic numbers (Mn_y and Mn_z) and Rayleigh number (Ra) on fluid flow, melting heat transfer and energy storage characteristics are illustrated and discussed. Results show that the applying a magnetic field parallel to buoyancy (z-direction) can effectively promote NEPCM melting. At low Ra, with an increase in the Mn, the complete melting time of NEPCM is shortened, and the heat storage efficiency can be increased by up to 4.613%, whereas the heat storage capacity is reduced by 2.814%. The competitive effect of dual-directional magnetic fields can effectively modify this mechanism. When natural convection is weak, the regulation of NEPCM melting by a magnetic field orthogonal to buoyancy (y-direction) exhibits a specific force-loop phenomenon. Under the coupled regulation of dual-directional magnetic fields, a new magnetic-force phenomenon emerges, in which the competition between the z- and y-direction magnetic fields disrupts the original force-loop structure of the Kelvin force. At high Ra, the magnetic field cannot change the vortex morphology, and the heat storage efficiency can be increased by up to 12.9%, with the heat storage capacity improved by 5.7%.

Keywords: Dual-directional Helmholtz coil magnetic fields, Vortex formation, Kelvin force, Metal foam, Nano-enhanced phase change material.

1. Introduction

Renewable energy systems play a crucial role in addressing global energy security and ecological environment issues [1]. To mitigate the mismatch between energy supply and demand caused by the intermittency of renewable energy, efficient thermal energy storage technologies are required. Latent heat thermal energy storage (LHTES) technology based on phase change materials (PCMs) can absorb or release a large amount of latent heat through the phase change process. When the supply of renewable energy is difficult to match in terms of time and space, LHTES technology holds great potential in optimizing energy management and controlling energy spillage [2]. Owing to its characteristics of high energy storage density and resistance to thermal shock, LHTES technology is expected to be applied in fields of precision electronic device [3], battery thermal management [4], waste heat recovery system, and spacecraft thermal control [5]. However, problems such as the poor thermal conductivity of phase change materials and the difficulty in regulating the phase change heat transfer process have become bottlenecks restricting the development of this technology. Currently, improving the thermal performance of PCMs and using external physical fields to assist phase change heat transfer are two important approaches to enhance the energy conversion and storage efficiency of LHTES technology [6].

To address the low thermal conductivity of PCM, researchers confirm that porous metal foams made of high thermal conductivity materials can achieve more uniform heat transfer enhancement in composite phase change systems [7]. The selection of porosity and pores per inch (PPI) for metal foams depends on whether the system prioritizes rapid heat storage or high heat storage capacity [8]. Contact between metal foam and phase change materials effectively enhances thermal conduction, but the structure of metal foam inevitably suppresses convective heat transfer, to a certain extent [9]. On the other hand, nanoparticles are also effective for improving internal heat transfer in PCMs [10]. Haidari et al. [11] numerically studied forced convective heat transfer of composite nanofluids in channels, noting that weakened convection was related to viscosity effects. Interactions between nanoparticles and the liquid phase of PCM may induce complex non-Newtonian rheological behavior, leading to uneven local heat

Published online: September 22 2026

transfer, more complex temperature gradient distribution, and altered melting behavior [2, 12]. Therefore, in the application of nano-enhanced PCMs, attention must be paid not only to the improvement of thermal conductivity by nanoparticles but also to their impact on the rheological properties of the material.

In recent years, the effects of external physical fields such as ultrasonic, electric, and magnetic fields on phase change heat transfer have attracted increasing attention. Proactively introducing external physical fields to regulate phase change heat transfer can improve the controllability of the phase change process, achieve on-demand regulation of energy storage characteristics, and solve various problems in multiple application scenarios. Ultrasonic fields promote the mixing and disturbance of liquid nano-enhanced PCMs in three-dimensional space through acoustic streaming, increasing flow velocity and enhancing convective heat transfer. Ultrasonic fields also generate microbubbles through cavitation [13]. These bubbles expand, compress, and eventually collapse under alternating positive and negative ultrasonic pressure, producing micro-jets, shock waves, and instantaneous high temperatures, thereby affecting the phase change process [14]. Among existing active heat transfer enhancement technologies, ultrasonic fields have been widely used to improve heat transfer performance during phase change. As for the electric field, electro-convection can be driven by Coulomb forces acting on dielectric media with free charges. In latent heat storage systems, heat transfer enhancement mainly stems from two mechanisms: electro-convection driven by Coulomb forces [15, 16], and solid-phase precipitation induced by dielectrophoretic forces at the phase change interface [17, 18].

Compared with the aforementioned external physical fields, magnetic fields offer bidirectional regulation to either suppress or promote phase change heat transfer, enable control of mass transport, and provide faster response [19-21]. For magnetic nanofluids, magnetic moments experience torque under a magnetic field, aligning particles along magnetic induction lines and magnetizing the fluid [22]. Studies on charged particles show that increasing magnetic parameters reduces fluid velocity while increasing fluid temperature [23]. An increase in Prandtl number enhances the magnetic field's influence on the flow field, while the effect on the average Nusselt number becomes weaker under a magnetic field [24]. The characteristics of non-uniform magnetic fields result in strong magnetic forces acting on the wall near the magnetic source, generating intense near-wall vortices during the melting of phase change materials to promote the mixing of hot and cold fluids [25]. The magnetic field arrangement of a Halbach array concentrates the strong magnetic field on one side of the magnet, effectively reducing interference from the magnetic field on unrelated components [26].

The magnetic field regulation on phase change heat transfer is influenced by the coupling of multiple factors, including PCM properties, magnetic field parameters, and nanoparticle parameters. Zhuang et al. [27] found that gradient porosity filling of porous media induced a competitive effect between thermal conduction and convective heat transfer, thereby affecting heat transfer and energy storage performance. Adding iron oxide nanoparticles improves the thermal conductivity of the composite but reduces its specific heat capacity and latent heat. Within an appropriate mass fraction range of 0 to 4 wt%, it can accelerate heat transfer and the phase change process [28]. After adding magnetic nanoparticles and applying a uniform external magnetic field, the heat transfer rate of the positive gradient porosity system is further enhanced. Li et al. [29] found that compared with pure PCMs, the melting time of such system was shortened by 64.29%, but the energy storage capacity was reduced by 16.44%. The addition of nanoparticles also induces non-Newtonian effects. Liu et al. [30, 31] focused on the synergistic effect of magnetic fields and composite nanoparticles on the phase change heat transfer behavior of non-Newtonian fluids. Xu et al. [32] found that magnetic Kelvin forces exhibited either force ring or force-bridge distributions at different Rayleigh numbers. Force-bridges weaken natural convection in the upper region and suppress heat transfer, while force rings homogenize the temperature distribution at the melting interface and promote heat transfer. Zhuang et al. [33] further studied magneto-convection during the melting of non-Newtonian ferrofluid nano-enhanced PCMs at low Rayleigh numbers, summarizing three stages of the phase change process and the formation mechanism and evolution of multi-vortex structures during melting. Some researchers have also explored the regulation mechanism from the perspective of different magnetic field directions. Ravari et al. [34] numerically studied the hydrodynamic instability of conductive viscous fluids in a cylindrical vessel considering the effect of an axial magnetic field. Dai et al. [35] attempted to generate an additional force field by applying a magnetic field on the four side walls of a square cavity, clarifying the mechanism of magnetic field regulation during the melting process. They showed that applying a magnetic field on the right wall suppressed melting, while applying it on the left and bottom walls promoted melting. However, single magnetic field regulation cannot achieve both high heat storage capacity and efficiency.

This study aims to explore the regulation mechanism of the coupling of dual-directional magnetic fields on the vortex modes, phase change heat transfer and energy storage performance of LHTES. Fe_3O_4 nanoparticles are dispersed in paraffin to form the NEPCM, which is subsequently filled into the pores of the copper foam to form the composite LHTES unit. Numerical simulations are carried out based on the enthalpy-porosity method, Darcy-Forchheimer model, and local thermal non-equilibrium model to investigate the melting process, non-Newtonian fluid flow, and heat transfer characteristics of NEPCM inside the LHTES. The time-dependent melting front, temperature field, velocity field, and Kelvin force field are obtained. The liquid fraction and Nusselt number over time, as well as the complete melting time and heat storage capacity under different cases, are also calculated and analyzed. A unidirectional magnetic field usually promotes the melting process at the cost of reduced total heat storage to achieve higher heat storage efficiency. In contrast, a dual-directional magnetic field balances the decrease in heat storage and the increase in heat storage efficiency through magnetic field competition, which enables more precise dynamic regulation. This study may provide a theoretical basis for optimizing specific engineering system performance, such as thermal management of unmanned aerial vehicles, building energy efficiency, and spacecraft thermal control.

2. Mathematical Model

2.1. Problem statement

Figure 1 presents a three-dimensional rectangular computational domain as the physical model of the LHTES unit. Two uniform Helmholtz coil magnetic fields are located outside the rectangular cavity, one is parallel to the y-axis with a magnetic induction intensity of B_y and the other is parallel to the z-axis with a magnetic induction intensity of B_z. These can generate the magnetic field force $\boldsymbol{F_k}$ acting on the liquid phase of NEPCM. The interior of the cavity contains NEPCM embedded with copper foam which has homogeneous porosity of 0.92 and 25 PPI. The left sidewall of the cavity serves as a heat source with a constant temperature T_h, while the remaining surfaces are kept adiabatic. The relevant thermophysical parameters of the paraffin wax, copper foam, and Fe_3O_4 nanoparticles used in this study are listed in Table 1, and the specifications of these materials are consistent with those in the literature [32, 36]. Among them, the melting temperature range of paraffin wax is T_m = 300.81 K to T_{m2} = 307.5 K [36]. The thermophysical properties of copper foam and Fe_3O_4 nanoparticles are taken as those of copper and Fe_3O_4, respectively, as reported in the literatures [37, 38].

Table 1. Thermophysical properties of Paraffin, Copper and Fe_3O_4 [32, 36].

Properties	Units	Paraffin	Copper	Fe_3O_4
Density	kg/m³	780 (liquid)	8920	5200
Dynamic viscosity	kg/(m·s)	0.00385	-	-
Specific heat capacity	J/(kg·K)	2196	380	670
Latent heat	kJ/kg	119.40	-	-
Thermal expansion coefficient	K^{-1}	0.00091	-	-
Thermal conductivity	W/(m·K)	0.23 (solid) 0.1 (liquid)	401	80
Melting point	K	300.81-307.5	-	-

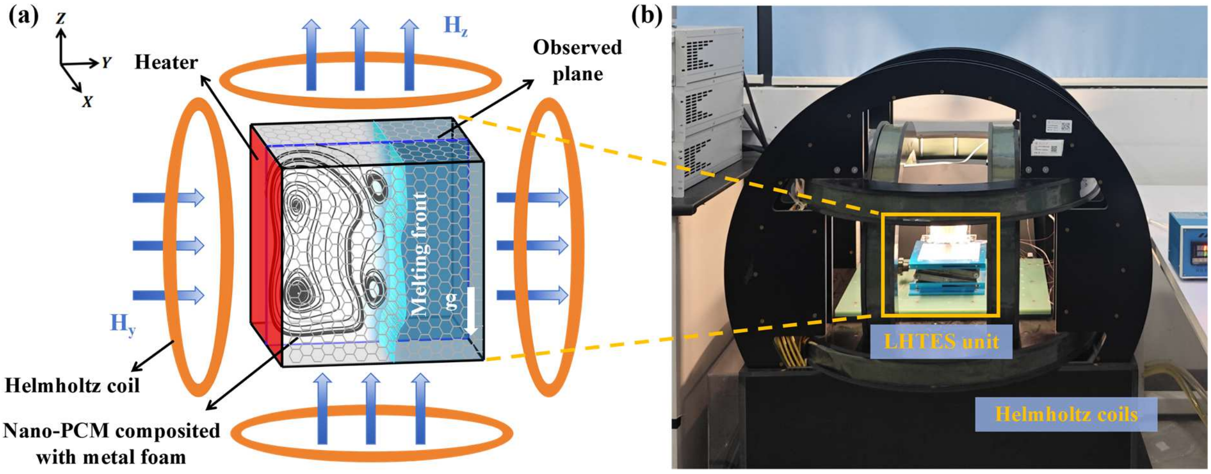

Fig. 1. Schematic diagram of the LHTES unit, (a) physical model of the LHTES unit, (b) overview of the experimental apparatus.

To establish the mathematical model, several important assumptions are clarified as follows:

(1) The liquid phase of paraffin is regarded as an incompressible fluid. The density change of liquid paraffin follows the Boussinesq approximation, and its viscosity change follows the power-law model [12]. Nanoparticles and phase change material are assumed to be fully mixed and in local thermal equilibrium. The variations in specific heat capacity, thermal conductivity and latent heat of paraffin during melting are neglected [39].

(2) The influence of the magnetic field on the viscosity of the nanofluid is neglected. The residual magnetic flux density is assumed to be non-existent. The base fluid (paraffin) of NEPCMs is treated as an insulator, which means no conduction current is generated in the fluid. Due to the narrow temperature variation range during the melting process, the relationship between magnetization and temperature can be considered linear [40].

(3) The copper foam and paraffin are treated as continuous media. The interaction between the magnetic field and the metal foam is neglected. The local thermal non-equilibrium (LTNE) model is adopted to describe the transient thermal energy interaction between paraffin wax and copper foam [41]. The Darcy model generalized by Forchheimer is applied to the conservation of the momentum equations [42].

2.2. Governing equations

Based on the volume-averaged conservation equations [42] for flow in porous media, the enthalpy-porosity method [43] for solid-liquid phase change, the Darcy-Forchheimer model [36] for porous resistance, and the LTNE model [41] for heat transfer between the NEPCM and copper foam, the governing equations can be written as follows:

Continuity equation:

$$\nabla \cdot \mathbf{U} = 0 \tag{1}$$

Momentum equations:

$$\frac{\rho_{nf}}{\varphi}\frac{\partial \mathbf{U}}{\partial t} + \frac{\rho_{nf}}{\varphi^2}\nabla\cdot(\mathbf{UU}) = -\nabla p + \frac{1}{\varphi}\nabla\tau - \left(\frac{\mu_{eff}}{K} + \frac{\rho_{nf}C}{\sqrt{K}}\|\mathbf{U}\|\right)\mathbf{U} - S_T\mathbf{U} + \mathbf{F_k} + (\rho\beta)_{nf}(T_{nf} - T_\infty)\mathbf{g} \tag{2}$$

Energy equations:

For paraffin:

$$\varepsilon\left[(\rho c_p)_{nf} + (\rho L)_{nf}\frac{d(f)}{d(T_{nf})}\right]\frac{\partial T_{nf}}{\partial t} + (\rho c_p)_{nf}\mathbf{U}\cdot\nabla T_{nf} = k_{nfe}\nabla^2 T_{nf} + h_{sf}a_{sf}(T_s - T_{nf}) \tag{3}$$

For copper foam:

$$(1-\varepsilon)(\rho c_p)_s\frac{\partial T_s}{\partial t} = k_{se}\nabla^2 T_s - h_{sf}a_{sf}(T_s - T_{nf}) \tag{4}$$

The terms on the right-hand side of Eq. (2) represent the pressure gradient, viscous stress, Darcy-Forchheimer resistance, mushy-zone resistance, Kelvin force, and buoyancy force, respectively. Their detailed formulations are provided below.

Table 2. Relevant parameters corresponding different volume fractions [32].

Volume fraction, Φ	0	0.00155	0.00465	0.00788
Mass fraction, Φ_{wt}	0%	1%	3%	5%
Power-law index, n	1	0.610	0.589	0.522

Where $\mathbf{U} = (u,v,w)$ indicates the corresponding velocity components in x, y and z directions, respectively. Here ε denotes the porosity of the copper foam, f is the local liquid fraction of the NEPCM within the pores, and $\varphi = \varepsilon f$ represents the volumetric liquid fraction in the composite domain. Therefore ε characterizes the geometrical pore space of the metal foam, whereas φ additionally accounts for the solid-liquid phase state of the NEPCM. It should be noted that φ and ε have different physical meanings and are therefore not interchangeable. t, p and g are the time, pressure and gravity acceleration, respectively. T_{nf}, T_s and T_∞ are the temperatures of NEPCM, copper foam and external environment, respectively. T_∞ is equal to 298K. ρ_s and c_s indicate density and specific heat capacity of copper paraffin, respectively. ρ_{nf}, c_{nf}, β_{nf} and L_{nf} are density, specific heat capacity, thermal expansion coefficients and latent heat of liquid NEPCM, respectively [12]:

$$\begin{bmatrix} \rho_{nf} \\ (\rho\beta)_{nf} \\ (\rho c)_{nf} \\ (\rho L)_{nf} \end{bmatrix} = (1-\Phi)\begin{bmatrix} \rho_f \\ (\rho\beta)_f \\ (\rho c)_f \\ (\rho L)_f \end{bmatrix} + \Phi \begin{bmatrix} \rho_{np} \\ (\rho\beta)_{np} \\ (\rho c)_{np} \\ 0 \end{bmatrix} \tag{5}$$

where physical quantities with subscripts f and np indicate the thermophysical parameters of PCM and nanoparticles, respectively. Φ is the volume fraction of nanoparticles in NEPCM. The expression of Φ_{wt} can be converted by Φ:

$$\Phi_{wt} = \frac{\rho_{np}\Phi}{\rho_{np}\Phi + (1-\Phi)\rho_f} \tag{6}$$

The second term of the right-hand side of the momentum Eq. (2) is the shear stress tensor τ. It describes the flow characteristic of non-Newtonian NEPCMs in liquid phase following the power-law model [44, 45]:

$$\tau_{ij} = 2\mu_{eff}\mathbf{D} \tag{7}$$

$$\mathbf{D} = \frac{1}{2}\left[\nabla\mathbf{U} + (\nabla\mathbf{U})^T\right] \tag{8}$$

$$\mu_{eff} = \mu_{nf}\left(2\mathbf{D}:\mathbf{D}\right)^{(n-1)/2} \tag{9}$$

where n is a power-law index. Table 2 shows the corresponding Φ_{wt} and n for NEPCM at different Φ. This work focuses on the regulation mechanism of the magnetic field on the melting process. Considering the universality of the Brinkman model, the effective viscosity μ_{eff} of the liquid power-law nano-enhanced phase change material and the viscosity μ_{nf} of the liquid NEPCM are calculated by Brinkman model [46]:

$$\mu_{nf} = \frac{\mu_f}{(1-\Phi)^{2.5}} \tag{10}$$

where μ_f is dynamic viscosity of liquid PCMs.

The third term of the right-side of the momentum Eq. (2), i.e., $((\mu_{eff}/K) + (\rho_{nf}C\|U\|/\sqrt{K}))\mathbf{U}$, is the expression of the Forchheimer extended Darcy model, which is used to characterize the non-Darcy and inertial effects induced by porous media during fluid flow [42]. K and C are permeability and inertia coefficient, respectively [47]:

$$K = \frac{\varepsilon^2}{36\chi(\chi-1)}d_k^2 \tag{11}$$

$$C = 0.00212(1-\varepsilon)^{-0.132}\left(\frac{d_f}{d_p}\right)^{-1.63} \tag{12}$$

where χ, d_k, d_f, and d_p denote the tortuosity coefficient, characteristic length, pore size and fiber diameter of copper foam, respectively:

$$\chi = 2 + 2\cos\left[\frac{4\pi}{3} + \frac{1}{3\cos(2\varepsilon - 1)}\right] \tag{13}$$

$$d_k = \frac{\chi d_p}{3-\chi} \tag{14}$$

$$d_f = 1.18 d_p\sqrt{\frac{1-\varepsilon}{3\pi}} \tag{15}$$

$$d_p = \frac{22.4 * 10^{-3}(m)}{\omega(PPI)} \tag{16}$$

The fourth term on the right-hand side of the momentum Eq. (2), i.e., $S_T\mathbf{U}$ is used to represent the effect of the mushy zone around the melting front on momentum exchange [43]:

$$S_T = A_{mush}\frac{(1-f)^2}{f^3 + 1\times 10^{-4}} \tag{17}$$

where A_{mush} is the mush zone constant, which significantly affects the shape of the solid-liquid interface. Based on the consistent agreement between numerical simulations and experimental results, it is set to 106 in the current work [48]. f indicates the liquid fraction in the pore:

$$f = \begin{cases} 0, & T_{nf} < T_{m1}, \\ \dfrac{T_{nf} - T_{m1}}{T_{m2} - T_{m1}}, & T_{m1} \le T_{nf} < T_{m2}, \\ 1, & T_{nf} \ge T_{m2} \end{cases} \tag{18}$$

Here, the liquid fraction for paraffin is jointly decided by f and porosity ε as $\varphi = \varepsilon f$.

The fifth term on the right-hand side of the momentum Eq. (2), i.e. $\mathbf{F_k}$ is the Kelvin body force source term. Since the paraffin base fluid of the NEPCM is electrically insulating, no conduction current is generated in the liquid phase. Therefore, the Lorentz force associated with electrical conduction is neglected, and the effect of the applied magnetic field on the liquid NEPCM is described solely by the ferrohydrodynamic (FHD) effect, represented by the Kelvin force. During melting, the magnetic nanoparticles dispersed in the liquid NEPCM are magnetized by the external magnetic field, and the resulting Kelvin force acts as a body-force source in the momentum equation. The Kelvin force is expressed as [32]:

$$\mathbf{F_k} = \mu_0 x_m(\mathbf{H}\cdot\nabla)(1+x_m)\mathbf{H} = \mu_0\mathbf{H}x_m(\mathbf{H}\cdot\nabla)(1+x_m) + \mu_0(1+x_m)(\mathbf{H}\cdot\nabla)\mathbf{H} \tag{19}$$

where μ_0 and $\mathbf{H}$ are the permeability of vacuum and the external magnetic field intensity vector, respectively. x_0 denotes the reference magnetic susceptibility, and the functional relationship between the magnetic susceptibility x_m of the NEPCM and the temperature T_{nf} is $x_m = x_0 / (1+\beta_{nf}(T_{nf} - T_\infty))$.

Since the uniform magnetic field in this study, $\mu_0(1+x_m)(\mathbf{H}\cdot\nabla)\mathbf{H} = 0$. Then the change in magnetic force is determined by the change in magnetic susceptibility. In other words, if the external magnetic field is uniform, the Kelvin force depends on the temperature gradient. In addition, the superparamagnetism of Fe_3O_4 nanoparticles will cause the direction of the magnetization to be consistent with the direction of the external magnetic field. Thus, the direction of the resulting Kelvin force is parallel to the y-axis and z-axis. The final form of the Kelvin force is expressed as:

$$\mathbf{F_K} = -\mu_0\mathbf{H}^2\frac{\beta_{nf}x_0^2}{\left[1+\beta_{nf}(T_{nf} - T_\infty)\right]^3}\frac{\partial T}{\partial y}\mathbf{j} - \mu_0\mathbf{H}^2\frac{\beta_{nf}x_0^2}{\left[1+\beta_{nf}(T_{nf} - T_\infty)\right]^3}\frac{\partial T}{\partial z}\mathbf{k} \tag{20}$$

The sixth term on the right-hand side of the momentum Eq. (2) is the buoyancy source term, where the density follows Boussinesq approximation:

$$\rho = \rho_\infty\left[1+\beta_{nf}(T - T_\infty)\right] \tag{21}$$

In energy equations with local non-thermal equilibrium, a tetrakaidecahedron effective thermal conductivity model of saturated porous metal foam established by Boomsma and Poulikakos [49] is employed to obtain effective thermal conductivity k_{eff} :

$$k_{eff} = \frac{1}{\sqrt{2}\left(R_A + R_B + R_C + R_D\right)} \tag{22}$$

$$R_A = \frac{4\sigma}{\left[2e^2 + \pi\sigma(1-e)\right]k_s + \left[4 - 2e^2 - \pi\sigma(1-e)\right]k_{nf}} \tag{23}$$

$$R_B = \frac{(e-2\sigma)^2}{(e-2\sigma)e^2 k_s + \left[2e - 4\sigma - (e-2\sigma)e^2\right]k_{nf}} \tag{24}$$

$$R_C = \frac{\sqrt{2} - 2e}{\sqrt{2}\pi\sigma^2 k_s + \left(2 - \sqrt{2}\pi\sigma^2\right)k_{nf}} \tag{25}$$

$$R_D = \frac{2e}{e^2 k_s + \left(4 - e^2\right)k_{nf}} \tag{26}$$

$$k_{nfe} = k_{eff}\Big|_{k_s = 0} \tag{27}$$

$$k_{se} = k_{eff}\Big|_{k_{nf} = 0} \tag{28}$$

where σ and e are dimensionless constants expressed as $\sigma = \sqrt{\sqrt{2}(2 - 3\sqrt{2}\,e^3/4 - 2\varepsilon)/\pi(3 - 2\sqrt{2}e - e)}$, $e = 0.16$. k_{nfe} and k_{se} are the effective thermal conductivities of NEPCMs and copper foam, respectively. k_{nf} and k_s represent the thermal conductivities of NEPCMs and copper foam, respectively. k_{nf} depends on the thermal conductivities of both pure PCM (k_f) and Fe_3O_4 nanoparticles (k_{np}), which follows the Maxwell's model [50]:

$$k_{nf}=k_f\frac{k_{np}+2k_f-2\Phi(k_f-k_{np})}{k_{np}+2k_f+\Phi(k_f-k_{np})} \tag{29}$$

At the microscopic pore scale, the significant enhancement of the liquid phase NEPCM heat transfer performance by the metal foam is non-negligible. Therefore, the thermal dispersion conductivity k_{td} can be calculated by Georgiadis and Catton's model [51]:

$$k_{td}=\frac{0.36}{1-\varepsilon}\rho_{nf}c_{nf}d_f\sqrt{u^2+v^2+w^2} \tag{30}$$

The h_{sf} and a_{sf} in second term at right-hand side of the Eqs. (3) and (4) denote the interfacial heat transfer coefficient and the interfacial surface area, respectively, which can be calculated based on Zhukauskas [52] as follows:

$$h_{sf}=\begin{cases}0.76Re^{0.4}Pr^{0.37}\dfrac{k_{nf}}{d_f}, & 0\le Re\le 40,\\ 0.52Re^{0.5}Pr^{0.37}\dfrac{k_{nf}}{d_f}, & 40<Re\le 10^3,\\ 0.26Re^{0.6}Pr^{0.37}\dfrac{k_{nf}}{d_f}, & 10^3\le Re\le 2\times 10^5\end{cases} \tag{31}$$

$$a_{sf}=\frac{3\pi d_f}{d_p^2} \tag{32}$$

The dimensionless parameters are defined as follows [12, 32]:

$$X=\frac{x}{d_k},Y=\frac{y}{d_k},Z=\frac{z}{d_k},U=\frac{ud_k}{\alpha_{nf}},V=\frac{vd_k}{\alpha_{nf}},W=\frac{wd_k}{\alpha_{nf}},Fo=\frac{t\alpha_{nf}}{d_k^2},P=\frac{pd_k^2}{\rho_f\alpha_{nf}^2},\theta=\frac{T_{nf}-T_\infty}{T_h-T_\infty},S_\theta=\frac{S_Td_k^2}{\rho_{nf}\alpha_{nf}},Sp=\frac{h_{sf}a_{sf}d_k^2}{(\rho C_p)_{nf}\alpha_{nf}},Mn=\frac{\mu_0H^2d_k^2}{\alpha_{nf}^2\rho_{nf}},$$
$$\nu=\left(\frac{\mu_f}{\rho_f}\right)^{\frac{1}{2-n}}*d_k^{\frac{2(1-n)}{2-n}},\ \xi=\frac{\alpha_{nf}}{\alpha_s},\xi_\rho=\frac{\rho_{nf}}{\rho_s},\xi_{cp}=\frac{(C_p)_{nf}}{(C_p)_s},Da=\frac{K}{d_k^2},Ste=\frac{(C_p)_{nf}\Delta T}{L_{nf}},Pr=\frac{\nu}{\alpha_{nf}},Ra=\frac{gd_k^3\beta_{nf}\Delta T}{\nu\alpha_{nf}},Re=\frac{u_m\rho_{nf}d_k}{\mu_{eff}} \tag{32}$$

Here $\alpha_{nf}=(k_{td}+k_{nfe})/\rho_{nf}c_{nf}$ and $\alpha_s=k_{se}/\rho_{nf}c_{nf}$ are the effective thermal diffusivities of NEPCM and copper foam, respectively. $u_m=\sqrt{u^2+v^2+w^2}$ is the characteristic velocity. Mn, Da, Ste, Pr, Ra and Re represent the Magnetic number, Darcy number, Stefan number, Prandtl number Rayleigh number and Reynolds number, respectively.

Then, Eqs. (1)-(4) can be expressed dimensionless as:

$$\nabla\cdot\dot{U}=0 \tag{33}$$

$$\frac{1}{\varphi}\frac{\partial U}{\partial Fo}+\frac{1}{\varphi^2}\left(U\frac{\partial U}{\partial X}+V\frac{\partial U}{\partial Y}+W\frac{\partial U}{\partial Z}\right)=-\frac{1}{E}\frac{\partial P}{\partial X}+\frac{FPr^*}{\varphi E}\left(\frac{\partial\tau_{XX}}{\partial X}+\frac{\partial\tau_{XY}}{\partial Y}+\frac{\partial\tau_{XZ}}{\partial Z}\right)-\left(\frac{F\bar{\mu}Pr^*}{EDa}+\frac{C}{\sqrt{Da}}\sqrt{U^2+V^2+W^2}\right)U-S_\theta U \tag{34}$$

$$\frac{1}{\varphi}\frac{\partial V}{\partial Fo}+\frac{1}{\varphi^2}\left(U\frac{\partial V}{\partial X}+V\frac{\partial V}{\partial Y}+W\frac{\partial V}{\partial Z}\right)=-\frac{1}{E}\frac{\partial P}{\partial Y}+\frac{FPr^*}{\varphi E}\left(\frac{\partial\tau_{XY}}{\partial X}+\frac{\partial\tau_{YY}}{\partial Y}+\frac{\partial\tau_{ZY}}{\partial Z}\right)-\left(\frac{F\bar{\mu}Pr^*}{EDa}+\frac{C}{\sqrt{Da}}\sqrt{U^2+V^2+W^2}\right)V-S_\theta V-\bar{M}\cdot Mn\frac{\partial\theta_{nf}}{\partial Y} \tag{35}$$

$$\frac{1}{\varphi}\frac{\partial W}{\partial Fo}+\frac{1}{\varphi^2}\left(U\frac{\partial W}{\partial X}+V\frac{\partial W}{\partial Y}+W\frac{\partial W}{\partial Z}\right)=-\frac{1}{E}\frac{\partial P}{\partial Z}+\frac{FPr^*}{\varphi E}\left(\frac{\partial\tau_{XZ}}{\partial X}+\frac{\partial\tau_{YZ}}{\partial Y}+\frac{\partial\tau_{ZZ}}{\partial Z}\right)-\left(\frac{F\bar{\mu}Pr^*}{EDa}+\frac{C}{\sqrt{Da}}\sqrt{U^2+V^2+W^2}\right)W-S_\theta W-\bar{M}\cdot Mn\frac{\partial\theta_{nf}}{\partial Z}$$
$$+Ra\cdot Pr\cdot\theta_{nf} \tag{36}$$

$$\left[\varepsilon+\frac{\varepsilon}{Ste}\frac{d(f)}{d(\theta_{nf})}\right]\frac{\partial\theta_{nf}}{\partial Fo}+\left(U\frac{\partial\theta_{nf}}{\partial X}+V\frac{\partial\theta_{nf}}{\partial Y}+W\frac{\partial\theta_{nf}}{\partial Z}\right)=\left(\frac{\partial^2\theta_{nf}}{\partial X^2}+\frac{\partial^2\theta_{nf}}{\partial Y^2}+\frac{\partial^2\theta_{nf}}{\partial Z^2}\right)+Sp(\theta_s-\theta_{nf}) \tag{37}$$

$$(1-\varepsilon)\frac{\partial\theta_s}{\partial Fo}=\frac{1}{\xi}\left(\frac{\partial^2\theta_s}{\partial X^2}+\frac{\partial^2\theta_s}{\partial Y^2}+\frac{\partial^2\theta_s}{\partial Z^2}\right)-\xi_\rho\xi_{cp}Sp(\theta_s-\theta_{nf}) \tag{38}$$

where $\bar{M}=\beta_{nf}\Delta T\chi_0^2/[1+\beta_{nf}\Delta T\theta_{nf}]^3$, $Pr^*=Pr^{2-n}$, and:

$$\bar{\mu}=\left[2\left(\frac{\partial U}{\partial X}\right)^2+2\left(\frac{\partial V}{\partial Y}\right)^2+2\left(\frac{\partial W}{\partial Z}\right)^2+\left(\frac{\partial U}{\partial Y}+\frac{\partial V}{\partial X}\right)^2+\left(\frac{\partial V}{\partial Z}+\frac{\partial W}{\partial Y}\right)^2+\left(\frac{\partial W}{\partial X}+\frac{\partial U}{\partial Z}\right)^2\right]^{\frac{n-1}{2}} \tag{39}$$

The ratio of density and viscosity between NEPCMs and foam copper can be defined as $E=\rho_{nf}/\rho_f=1-\Phi+\Phi\rho_f/\rho_{np}$, $F=\mu_{nf}/\mu_f=1/(1-\Phi)^{2.5}$.

In this study, the dimensionless side length of external cubic cavity is set as N. The boundary is impermeable, and no slip wall boundary condition is used in the simulations. The initial conditions are as follows:

$$Fo=0,\quad U=V=W=0,\quad \theta_{nf}=\theta_s=\theta_\infty=0,\quad \theta_h=1 \tag{40}$$

The boundary conditions of the cubical cavity are as follows:

$$Fo > 0; \quad Y = 0; \quad 0 \le X \le N; \quad 0 \le Z \le N; \quad \theta_{nf} = \theta_s = \theta_h = 1 \tag{41}$$

$$Fo > 0; \quad Y = N; \quad 0 \le X \le N; \quad 0 \le Z \le N; \quad \frac{\partial \theta_{nf}}{\partial X} = \frac{\partial \theta_{nf}}{\partial Z} = \frac{\partial \theta_s}{\partial X} = \frac{\partial \theta_s}{\partial Z} = 0 \tag{42}$$

$$Fo > 0; \quad X = 0 \text{ or } N; \quad 0 \le Y \le N; \quad 0 \le Z \le N; \quad \frac{\partial \theta_{nf}}{\partial Y} = \frac{\partial \theta_{nf}}{\partial Z} = \frac{\partial \theta_s}{\partial Y} = \frac{\partial \theta_s}{\partial Z} = 0 \tag{43}$$

$$Fo > 0; \quad Z = 0 \text{ or } N; \quad 0 \le X \le N; \quad 0 \le Y \le N; \quad \frac{\partial \theta_{nf}}{\partial X} = \frac{\partial \theta_{nf}}{\partial Y} = \frac{\partial \theta_s}{\partial X} = \frac{\partial \theta_s}{\partial Y} = 0 \tag{44}$$

2.3. Heat transfer and energy storage

In the present research, the impact of convective heat transfer on the melting behavior of NEPCM is characterized by two key parameters of the fluid adjacent to the heating wall: the local Nusselt number (Nu) and the average Nusselt number ($\overline{Nu}$). Furthermore, to conduct a comprehensive assessment of NEPCM's heat storage performance, three non-dimensional indicators are incorporated: non-dimensional total heat storage (E^*), non-dimensional sensible heat storage (E_S^*), and non-dimensional latent heat storage (E_L^*). As for the energy storage efficiency (Q^*) throughout the entire phase change process, it can be quantified with the aid of two non-dimensional parameters, Fo_t and Q^* [32]:

$$Nu = -\left.\frac{\partial \theta_{nf}}{\partial Y}\right|_{Y=0} \tag{45}$$

$$\overline{Nu} = \int_{Z=0}^{L}\int_{X=0}^{L} |Nu|\, dX\, dZ \tag{46}$$

$$E(t) = E_{nf}(t) + E_s(t) \tag{47}$$

$$E_{nf}(t) = \begin{cases} m_{nf} c_{nf} \left(T_{ave}(t) - T_\infty\right), & T \le T_{m1} \\ m_{nf} c_{nf} \left(T_{nf\,ave}(t) - T_\infty\right) + m_{nf} L_{nf}, & T > T_{m1} \end{cases} \tag{48}$$

$$E_s(t) = m_s c_s \left(T_{save}(t) - T_\infty\right) \tag{49}$$

$$E_L(t) = m_{nf} L_{nf} \tag{50}$$

$$E_S(t) = m_{nf} c_{nf} \left(T_{nf\,ave}(t) - T_\infty\right) + m_s c_s \left(T_{save}(t) - T_\infty\right) \tag{51}$$

$$E^* = \frac{E}{E_{ref}}, \quad E_S^* = \frac{E_S}{E_{Sref}}, \quad E_L^* = \frac{E_L}{E_{Lref}} \tag{52}$$

$$Q = \frac{E(t_{total})}{t_{total}}, \quad Fo_t = \frac{Fo_{total}}{Fo_{totalref}}, \quad Q^* = \frac{Q}{Q_{ref}} \tag{53}$$

where the subscript '*ref*' denotes the reference case.

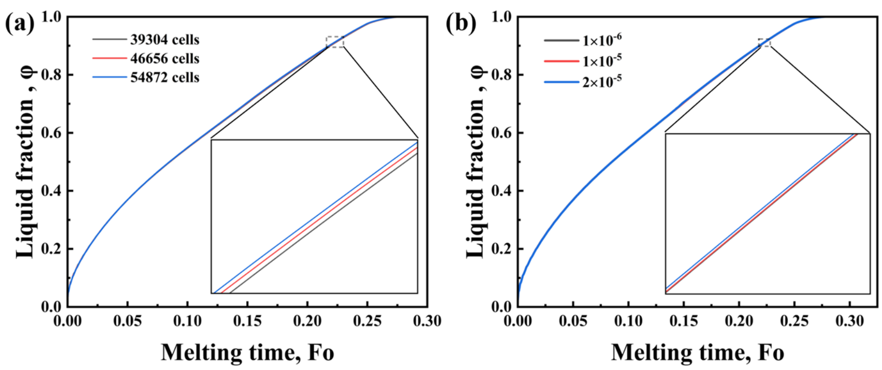

Fig. 2. Independent analyses under, (a) different grid numbers and, (b) time steps.

3. Numerical Method and Experimental Validation

3.1. Numerical method

In this research, the numerical simulation adopts an iterative finite volume method, which utilizes a three-dimensional staggered grid and is coupled with the Semi-Implicit Method for Pressure Linked Equations (SIMPLE) algorithm. Under the staggered grid setup, velocity components are assigned to the midpoints of cell faces (aligned perpendicularly to the components), whereas scalar properties like pressure and temperature are placed at the cell centers. For temporal discretization, the forward difference scheme is employed to approximate transient terms. Meanwhile, convective terms are discretized via the second-order upwind scheme, and diffusive terms via the central difference scheme. Additional specifics regarding the numerical approaches have been documented in our prior studies [27, 53].

Grid number and time step independence analyses are presented in Fig. 2. For the computational domain, different grid configurations (39,304, 46,656, and 54,872 cells) and different steps (1×10^{-6} s, 1×10^{-5} s and 2×10^{-5} s) were tested, respectively. Balancing computational efficiency and solution accuracy, the present study employs a 46,656 cells grid and a 1×10^{-5} s time step for simulating the phase change heat transfer process across all cases.

3.2. Experimental validation

Figure 3(a) presents the magnetic field experimental setup employed in this study, where the magnetic field directions are along the y-axis and z-axis. The complete experimental setup comprises a temperature regulator, thermocouples, a data logging module, a computer, an infrared camera, a direct current (DC) power supply, a gaussmeter, an oil cooler, an LED light source, and a Helmholtz coil. The test component subjected to a uniform magnetic field is a rectangular chamber (40 mm × 40 mm × 40 mm) fabricated from acrylic glass; this chamber is filled with NEPCM combined with copper foam. The Fe_3O_4 nanoparticles within the NEPCM have an average diameter of 20 nm and the mass fraction of 3 wt%. Mounted on the left wall of the chamber is an aluminum heater linked to the temperature regulator, designed to deliver continuous and uniform heating. Inside the chamber, 8 T-type thermocouples are placed at pre-determined positions, these thermocouples transmit real-time data on transient temperature fluctuations to the computer via the data logging module. To achieve effective thermal insulation, the chamber is wrapped with 30 mm-thick insulation pearl cotton around its sides and on its top. Prior to initiating the experiment, the magnetic field intensity in the vicinity of the chamber is calibrated using a gaussmeter (with an accuracy of ±2% mT), guaranteeing that the entire chamber is situated within a uniform magnetic field. Throughout the experiment, the DC power supply allows for adjustment of the current flowing through the coil, which in turn modulates the magnetic field intensity. The magnetic field intensity in the experiment is set to 60Gs in both the positive y-axis and positive z-axis. The experiment was conducted under the conditions where the room temperature was controlled at 25°C and the heating side was maintained at 70°C.

Figure 3(b) compares the evolution of the melting front in the magnetic field experimental system with the numerical simulation results. Both experimental and numerical results show that in the early melting stage (Fo = 0.02), the angle between the melting interface and the left wall is relatively small. This indicates that heat conduction plays a more significant role in the heat transfer process than natural convection during this period. With the elapse of time (Fo = 0.06-0.90), the continuous expansion of the liquid phase region allows natural convection which gradually dominates heat transfer to accelerate the melting of paraffin in the upper part of the square cavity, leading to a gradual tilt of the melting interface. At this point, the fluid tends to move upward due to the buoyancy force. Since temperature exerts a more significant influence on the upward tendency of the fluid on the left heating wall than on that at the solid-liquid interface on the right, the liquid phase region exhibits an overall clockwise flow, and the upper part of the solid phase region receives more momentum exchange and heat energy transfer. It should be noted that there are discrepancies in the melting interface profiles of the two results in the middle of the cavity: the turning point of the solid-liquid interface in this region is less distinct in the experimental results compared to the numerical simulation. Several factors may account for this phenomenon: First, the Forchheimer extended Darcy model may overstate the effect of natural convection. Additionally, the random selection of A_{mush} may introduce certain errors. Both of these factors lead to faster melting in the upper part during the numerical simulation.

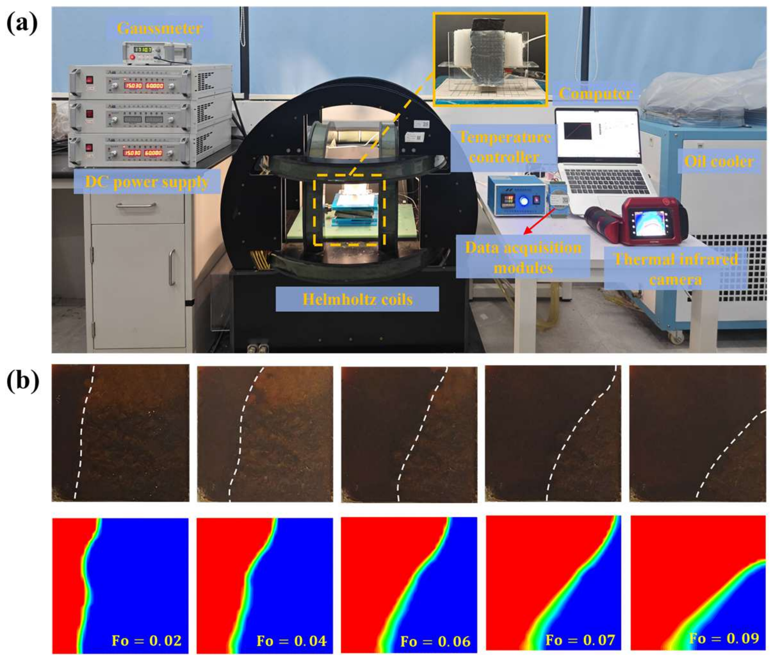

Fig. 3. (a) Helmholtz coil magnetic field experiment system, (b) Comparison of melting interface profiles between numerical and experimental results under a uniform magnetic field.

Second, the Brinkman model may, to a certain extent, underestimate the viscosity change of NEPCM [54], thereby causing deviations in the numerical results. Additionally, heat absorption by the insulation material and the incomplete uniformity of the porous medium structure during the experiment may impact the heat exchange in the melting process [55]. Nevertheless, the numerical results are in good agreement with the experimental results throughout the entire melting process, which verifies the reliability of the employed numerical model and computational code.

4. Results and Discussion

This study aims to investigate the melting dynamics of NEPCMs under the coupling effect of natural convection and dual-directional Kelvin magnetic forces. It focuses on exploring the influences of different Ra and Mn of dual-directional magnetic fields on the phase change heat transfer characteristics of LHTES unit. Firstly, the non-Newtonian melting behavior under the influence of different Mn of z-direction magnetic field at low Ra is compared. On this basis, the regulation mechanism of uniform magnetic fields on phase change heat transfer is studied under different Mn of the coupled y-direction and z-direction magnetic fields. Then, the characteristics of magnetic field regulation on magnetofluids at different Ra values are investigated, and results regarding different Kelvin force configurations are obtained. Driven by natural convection and magnetic convection, the three-dimensional model, which accounts for non-Newtonian effects and magnetic field effects, exhibits a quasi-two-dimensional flow field distribution. To more clearly demonstrate the evolution of the vortex structure in the liquid phase region during the melting process, the cross-section at x = 0.5 in the three-dimensional cavity is selected as the observation plane to present the two-dimensional results.

4.1. Effect of z-direction magnetic field on melting heat transfer

First, this section discusses the effect of a magnetic field parallel to buoyancy (z-direction magnetic field) on the phase change heat transfer of NEPCM. Figures 4(a) – 4(d) compare the performance of different Mn values at Fo = 0.08 and Ra = 10^3. The comparison is made from the perspectives of streamlines, temperature field, velocity field, and z-direction Kelvin force field, respectively.

In Fig. 4(a), it can be observed that after the introduction of the z-direction magnetic field, the flow field morphology evolves from a single large vortex into two vortices split vertically in the middle, with two additional small vortices formed. As Mn increases, the splitting of the large vortex becomes more pronounced, and the two accompanying small vortices also grow larger. Under the condition of $Mn_z = 7\times10^6$, the stronger z-direction Kelvin force almost splits the large vortex into a multi-vortex structure with 5 vortices. Figure 4(b) shows that without a magnetic field, the isotherms near the heat source in the temperature field are almost parallel. This indicates that heat conduction dominates the heat transfer in this region. However, the liquid NEPCM near the solid NEPCM continuously scours the solid phase region under the influence of natural convection. As a result, the solid-liquid interface here becomes wavy, causing the isotherms near the solid phase to start showing wavy changes. For the three magnetic field cases in Fig. 4(b), under the action of the magnetic field, the streamlines near the heat source are no longer parallel to the heat source. This leads to gradient changes in the vertical temperature. The wavy folds of the isotherms become more obvious as they approach the solid phase region. Moreover, the folds increase with the increase of Mn. Figure 4(c) shows that the velocity field evolves from a uniformly distributed single-vortex structure into a structure with four or even five vortices. Moreover, the introduction of the magnetic field significantly increases the overall velocity, which greatly enhances the heat transfer of the entire phase change system. Under all magnetic field conditions, two high-velocity zones corresponding to the vortex positions appear on the heating side. This is caused by the coupling of buoyancy-driven natural convection and Kelvin force-driven magnetic convection. As shown in Fig. 4(d), the Kelvin force induced by the z-direction magnetic field shows an overall sheet-like distribution. It also has a positive-negative alternating distribution pattern. As indicated in the Eq. (19), the Kelvin force is mainly related to the temperature gradient. The wavy folds of the temperature field in Fig. 4(b) provide a positive-negative alternating temperature gradient for the Kelvin force. This makes the Kelvin force show a positive-negative-positive-negative distribution pattern. Positive Kelvin forces exert an upward force on the liquid PCM, increasing its velocity. In contrast, negative Kelvin forces cause the velocity vector of the liquid PCM to deflect in advance. This further leads to the phenomenon where the large vortex is split into two small vortices from the middle in Fig. 4(c). The high-velocity zones shown in the velocity field are exactly the regions where the liquid PCM deflects. The low-velocity zones are mostly located at the centers or peripheries of the vortices.

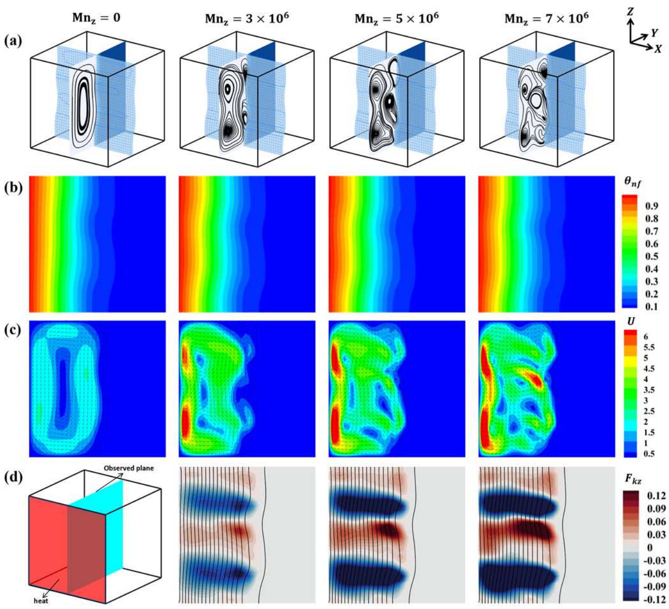

Fig. 4. Comparisons of (a) streamline, (b) temperature field θ_{nf}, (c) velocity field and, (d) z-direction Kelvin force field F_{kz} distributions for Mn_z from 0 to 7×10^6 at Fo = 0.08 and Ra = 10^3.

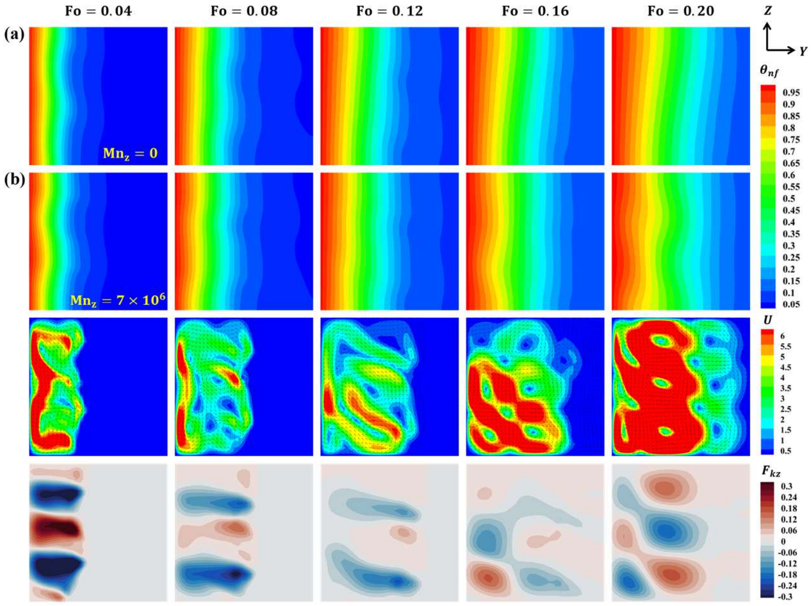

Fig. 5. Changes of temperature, velocity and z-direction Kelvin force distributions for, (a) $Mn_z = 0$ and, (b) $Mn_z = 7\times10^6$ with Fo at Ra = 10^3.

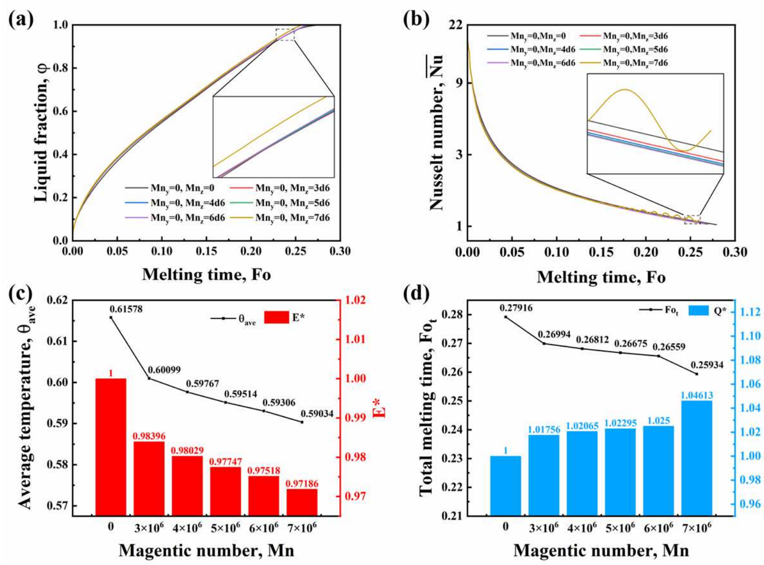

Fig. 6. (a) Variations of liquid fraction with Fo for different Mn, (b) Variations of average Nusselt number with Fo for different Mn, (c) Variations of average temperature and total heat storage for different Mn, (d) Variations of total melting time and heat storage efficiency for different Mn.

Figures 5(a) and 5(b) illustrate the development of the melting process from the early stage (Fo = 0.04) to the later stage (Fo = 0.20) without and with a magnetic field, respectively. Under the condition without a magnetic field, heat conduction dominates the heat transfer process in the early melting stage (Fo = 0.04). The isotherms on the heating side are nearly parallel, while those on the solid phase side only show slight waviness. As time progresses, the liquid phase region expands, and natural convection begins to play a role. Driven by natural convection, the upper part of the liquid phase region melts faster; eventually, in the late melting stage, the isotherms as a whole tilt to the right. At a high Mn_z, the interface of the solid phase region advances gradually to the right in a posture almost parallel to the heating side. For the interior of the liquid phase region, the introduction of the magnetic field leads to more intense temperature changes and larger variations in the internal temperature gradient.

Regarding the evolution of Kelvin force field, the z-direction Kelvin force initially presents a sheet-like distribution. As the melting proceeds, it evolves into a strip-like shape with a curved profile in the middle melting stage (Fo = 0.12), and the two negative Kelvin force regions begin to show a tendency to connect. In the middle-late melting stage (Fo = 0.16), the complex convective heat transfer process drives the high-temperature region at the bottom of the liquid PCM to move forward. Changes in the temperature gradient cause the negative Kelvin force regions to merge into a single area. In the late melting stage, the Kelvin force finally takes on an inclined dumbbell-like shape. The evolution of the Kelvin force field indicates that magnetic convection is continuously driven by a dynamically changing driving force with complex variations. From the velocity field, the Kelvin force dominates the changes in vortices throughout the process. The vortex structure evolves from a double-vortex structure at Fo = 0.04, to a multi-vortex structure at Fo = 0.12, and finally to a six-vortex stage at Fo = 0.20. Both the formation and evolution of vortices are associated with the changes in the morphology of the Kelvin force.

Figure 6(a) shows the variation of liquid fraction with time under different magnetic field intensities. Overall, the introduction of a magnetic field promotes the melting of NEPCMs. At low Ra, the buoyancy-driven natural convection is weak. For most of the time, the heat transfer process of the NEPCM phase change system is dominated by heat conduction. However, with the addition of a magnetic field, the fluid is driven by two forces. One is buoyancy-induced natural convection, and the other is Kelvin force-induced magnetic convection. This significantly facilitates the development of convection. The generation of magnetic convection increases the heat transfer rate of the entire NEPCM phase change system. Therefore, at low Ra, magnetic convection plays a decisive role in the melting rate. The melting rate increases as the Mn rises. As observed in Fig. 6(b), the $(\overline{Nu})$ under high Mn conditions exhibits fluctuations after the late melting stage. Such fluctuations may be attributed to the more prominent disturbance of the nanofluid on the heating wall caused by stronger magnetic forces, which disrupts the stable convective heat transfer. Figure 6(c) plots the average temperature and total heat storage under different magnetic field intensities, as the cases discussed in this section have the same latent heat. The heat storage efficiency shown in Fig. 6(d) is jointly determined by heat storage efficiency and total melting time. From the bar charts in Figs. 6(c) and 6(d), it can be seen that although the increase in Mn reduces heat storage, it leads to a much greater reduction in total melting time. Thus, increasing Mn effectively improves heat storage efficiency. This effect is particularly notable under high Mn conditions where convective heat transfer is more unstable. In terms of heat storage, the smallest Mn reduces total heat storage by 1.604%, and the largest Mn reduces it by 2.814%. For heat storage efficiency, the smallest Mn increases it by 1.756%, while the largest Mn increases it by 4.613%.

4.2. Coupling effects of y-z directional magnetic field

In the previous section, we found that the magnetic field parallel to buoyancy significantly promotes the melting behavior of NEPCM at low Rayleigh number. Magnetic convection induced by this magnetic field compensates for the low intensity of natural convection and forms a multi-vortex structure that accelerates the melting process. On this basis, this section further investigates the coupled effect of the z-direction magnetic field parallel to buoyancy and the y-direction magnetic field orthogonal to buoyancy on the melting of NEPCM at the current Rayleigh number.

Figure 7 presents streamline diagrams for the z-direction magnetic number Mn_z and y-direction magnetic number Mn_y ranging from 0 to 7×10^6. From the first row of Fig. 7, it can be observed that under the influence of the y-direction magnetic field alone, the single large vortex in the no-magnetic-field case differentiates into two longitudinal rows of vortices. This phenomenon becomes more pronounced as Mn_y increases. Under the highest Mn condition, an even structure of two uniform rows with 8 vortices in total appears. In contrast, the z-direction magnetic field mainly causes transverse vortex differentiation, which is consistent with the scenario discussed in the previous section. Under the coupled y-direction and z-direction magnetic fields, the streamlines exhibit four main morphologies: (1) Transversely differentiated vortices dominated by the z-direction magnetic field (yellow zone); (2) Longitudinally differentiated vortices dominated by the y-direction magnetic field (orange zone); (3) Single vortices resulting from competition between y- and z-direction magnetic fields (grey zone); (4) Vertical vortices resulting from competition between y-direction and z-direction magnetic fields (red zone). Under the influence of the y-direction magnetic field, the introduction of the z-direction magnetic field first disrupts the longitudinal vortex differentiation morphology induced by the y-direction magnetic field. For grey zone cases, neither the longitudinal differentiated vortices caused by the y-direction magnetic field nor the transverse differentiated vortices caused by the z-direction magnetic field are visible. This is because both magnetic fields are relatively weak. The disturbance from the z-direction magnetic field disrupts the original magnetic convection induced by the y-direction magnetic field. It alters the streamline morphology and eliminates the original vortices.

In the cases shown in the second row, as Mn_y increases, the z-direction magnetic field exerts an increasingly weaker disruptive effect on the formation of longitudinal vortices. This is due to the fragile nature of their competitive relationship: when Mn_y increases, the z-direction magnetic field loses its dominance over the flow field morphology to the y-direction magnetic field, leading to a return to the y-direction-dominated state. Similarly, in the case of grey zone, mutual competition between the two magnetic fields results in a vortex morphology closer to that of the no magnetic field case. When $Mn_y > Mn_z$, the morphology of most streamlines is similar to that under the y-direction magnetic field alone. Correspondingly, when $Mn_z > Mn_y$, the streamline morphology is mostly analogous to that under the z-direction magnetic field alone. This indicates that the streamline morphology is dominated by the magnetic field with the higher intensity between the two directions. The fifth and sixth columns of Fig. 7 show cases with $Mn_y = 6\times10^6$ and $Mn_y = 7\times10^6$. In these cases, the fourth vortex morphology, vertical vortices, can be observed. The formation of this morphology is attributed to the sufficiently strong y-direction magnetic field alone in these cases. This magnetic field intensity enables the formation of a relatively stable structure with 8 vortices. The subsequent introduction of the z-direction magnetic field exerts a compressive force on the fluid in another direction. This compression disrupts the original vortex structure while driving the fluid to flow in the x-direction. Eventually, the centers of the vortices shift from the original y-z plane to the x-y plane, forming vertical vortices.

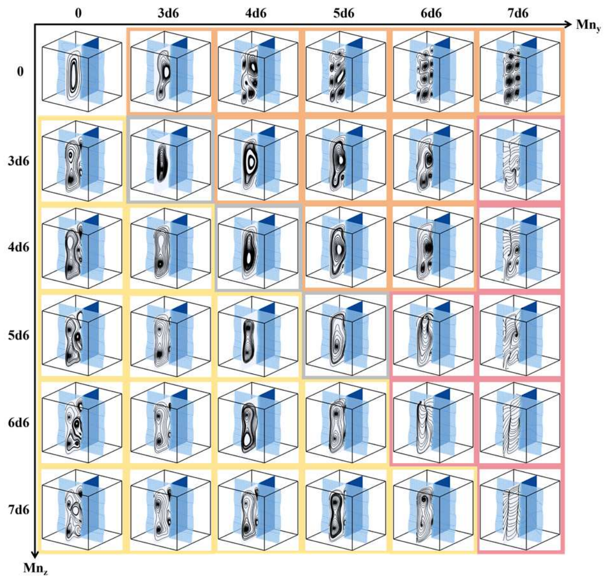

Fig. 7. Comparison of streamlines for Mn_z from 0 to 7×10^6 and Mn_y from 0 to 7×10^6 at Fo = 0.08 and Ra = 10^3.

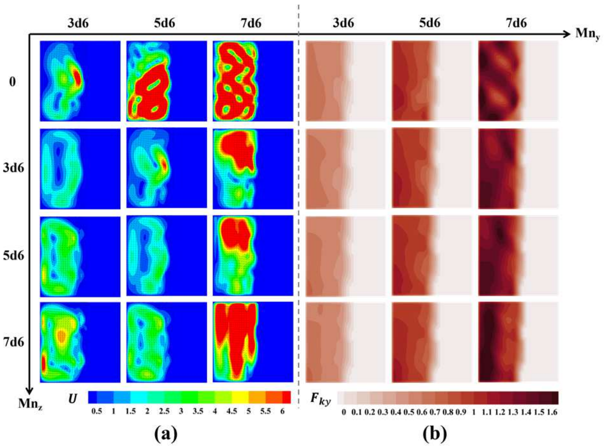

Fig. 8. Comparisons of (a) velocity field and, (b) y-direction Kelvin force field for Mn_y from 3×10^6 to 7×10^6 and Mn_z from 0 to 7×10^6 at Fo = 0.08 and Ra = 3×10^6.

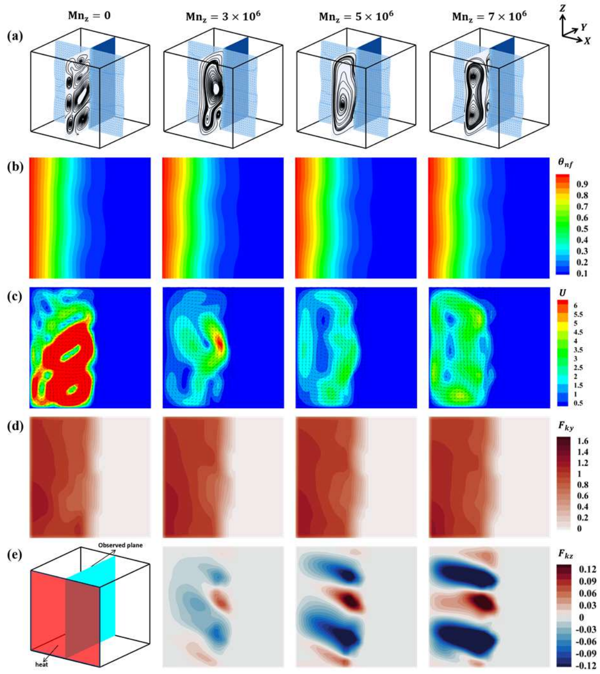

Fig. 9. Comparisons of (a) streamline, (b) temperature field, (c) velocity field, (d) y-direction Kelvin force field and (e) z-direction Kelvin force field distributions for Mn_z from 0 to 7×10^6 with $Mn_y = 5\times10^6$ at Fo = 0.08.

Figures 8(a) and 8(b) show the velocity field and y-direction Kelvin force field under different combinations of Mn_y and Mn_z, respectively. In the first row of cases where without z-direction magnetic field, the y-direction Kelvin force presents as force-loops [32]. These force-loops distribution enables the Kelvin force to influence a large portion of the liquid region, thereby enhancing convection within the molten NEPCM. From left to right, as Mn_y increases, the shape of these force-loops becomes increasingly distinct. The changes in the velocity field shown in Fig. 8(a) align with the previously analyzed effect of coupled y-direction and z-direction magnetic fields on streamlines. The introduction of the z-direction magnetic field disrupts the original streamline morphology induced by the y-direction magnetic field. Meanwhile, it also alters the morphology of the velocity field and the pattern of velocity distribution. In the case with the highest Mn_y, adding the z-direction magnetic field leads to the formation of vertical vortices. This explains why a large high-velocity region appears in the cases with the highest Mn_y and a z-direction magnetic field in Fig. 8(a).

For the y-direction Kelvin force field, the introduction of the z-direction magnetic field changes its morphology, and this is just like how it affects the streamlines and velocity field. In the series of cases with the highest Mn_y, it is evident that the y-direction Kelvin force field originally has clear force-loops when without z-direction magnetic field is applied. After adding a small z-direction magnetic field, multiple force-loops begin to merge. When the magnetic number of the z-direction magnetic field increases, the force-loops nearly vanish. When the magnetic number of the z-direction magnetic field reaches its maximum, the force-loops in the y-direction Kelvin force field disappear entirely. In their place are clearly divided regions: a high y-direction Kelvin force region on the left and a low y-direction Kelvin force region on the right, with an overall column-like shape.

Figures 9(a) to 9(e) show the streamline diagram, temperature field diagram, velocity field diagram, y-direction Kelvin force diagram, and z-direction Kelvin force diagram under different Mn_z values when $Mn_y = 5\times10^6$, respectively. As can be seen from Fig. 9(a), with the lowest Mn_z, the structure of two longitudinal rows of vortices generated by the y-direction magnetic field is disrupted. Seven of these vortices merge into a single large vortex. This disruption of the vortex structure is caused by the competition between the z-direction and y-direction magnetic fields. When Mn_z increases, the large vortex and small vortices continue to merge, resulting in an overall streamline morphology with only one vortex. This is because the y-direction and z-direction magnetic fields are evenly matched at this point. The vortex morphology neither shows characteristics influenced by the y-direction magnetic field nor the z-direction magnetic field. When Mn_z rises to maximum, the large vortex begins to split transversely, eventually forming two small vortices arranged in a transverse pattern. At this stage, the z-direction magnetic field dominates magnetic convection, so the vortex morphology exhibits characteristics affected by the z-direction magnetic field. From Fig. 9(b), it can be observed that the introduction of the z-direction magnetic field mainly affects the heating side. Comparing the isotherms on the heating side across the four working conditions, the z-direction magnetic field changes the isotherms on the heating side from straight lines to wavy shapes. This is consistent with the effect of the z-direction magnetic field on the temperature field analyzed in the previous section. For the solid side, however, the addition of the z-direction magnetic field has little impact when the y-direction magnetic field is present. The disruptive effect of the z-direction magnetic field on the y-direction magnetic field can be more clearly seen in the velocity field diagram of Fig. 9(c). The introduction of the z-direction magnetic field not only changes the streamline morphology but also reduces the overall velocity. The z-direction magnetic field with the lowest Mn_z causes the high-velocity region observed in the condition without the z-direction magnetic field to disappear completely. Figures 9(d) and 9(e) show the y-direction Kelvin force field and z-direction Kelvin force field, respectively. Comparing the two sets of diagrams, it can be seen that under this Mn_y value, the introduction of the z-direction magnetic field has no obvious impact on the y-direction Kelvin force field. In contrast, changes in the z-direction Kelvin force field are mostly related only to the magnitude of Mn_z. An increase in Mn_z only increases the numerical value of the z-direction Kelvin force and does not significantly alter the morphology of the z-direction Kelvin force field.

Figure 10 shows the z-direction Kelvin force field diagrams under different combinations of Mn_y and Mn_z parameters. The z-direction Kelvin force distribution in almost all working conditions follows the positive-negative-positive-negative pattern mentioned in the previous section. For the four groups of y-direction magnetic numbers, an increase in Mn_z can amplify the numerical value of the z-direction Kelvin force but has little impact on its morphology. Only in the two groups of working conditions with moderate Mn_y and the highest Mn_y, the regional differentiation of the z-direction Kelvin force field becomes more obvious after increasing Mn_z. For the three groups of z-direction magnetic numbers, in the two working conditions of the lowest Mn_z and moderate Mn_z, when Mn_y is greater than Mn_z, the z-direction Kelvin force field not only tilts but also tends to have two negative Kelvin force regions connected together. This is because Mn_y is stronger than Mn_z at this time, so the y-direction magnetic field plays a role in disrupting the morphology caused by the z-direction magnetic field. However, with the highest Mn_z, the morphology of the z-direction Kelvin force field is always determined by the z-direction magnetic field. Therefore, the introduction of the y-direction magnetic field can only cause tilting and will not change its morphology.

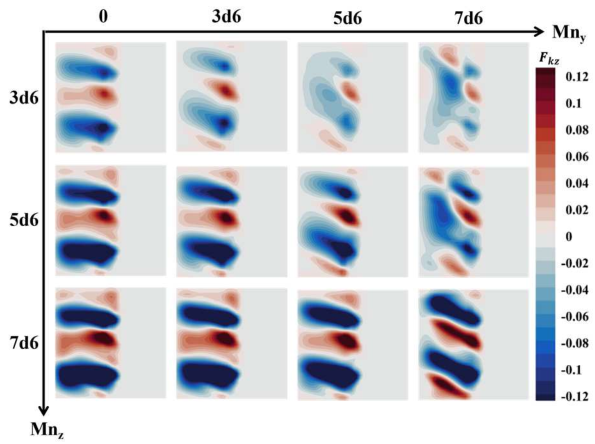

Fig. 10. Comparisons of z-direction Kelvin force field for Mn_y from 0 to 7×10^6 and Mn_z from 3×10^6 to 7×10^6 at Fo = 0.08 and Ra = 10^3.

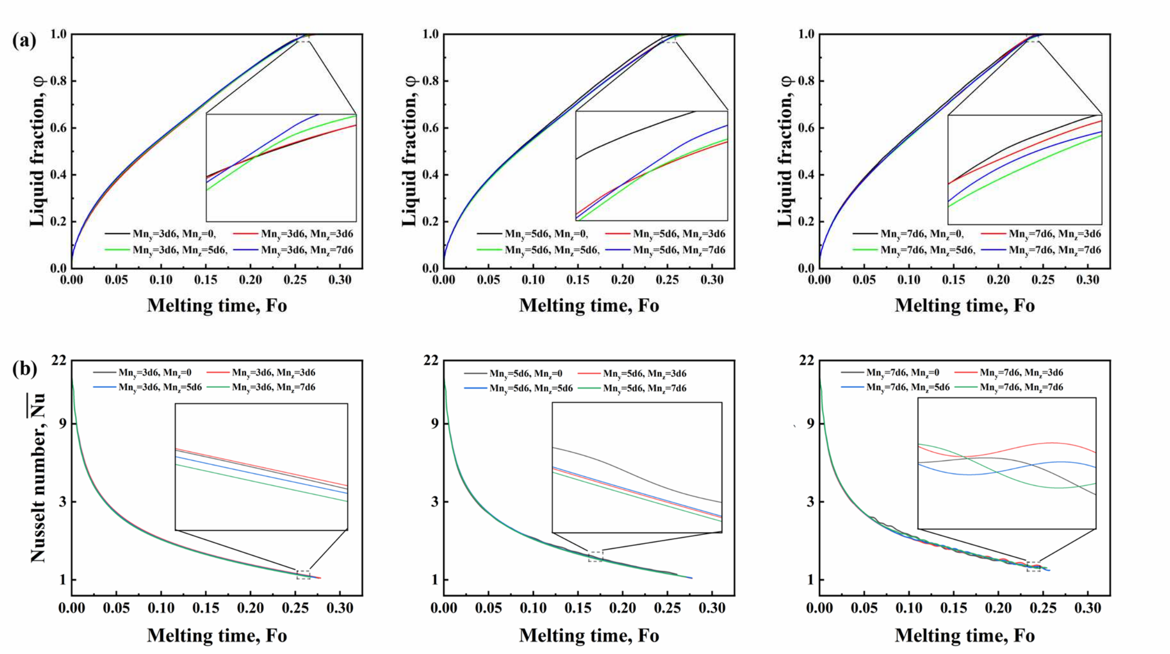

Fig. 11. (a) Variations of liquid fraction with Fo, (b) Variations of average Nusselt number with Fo for different Mn_y and Mn_z.

Figures 11(a) and 11(b) show the variation of liquid fraction with time and the variation of $(\overline{Nu})$ with time under different Mn_y and Mn_z parameters, respectively. From the liquid fraction variation diagram, it can be observed that when a y-direction magnetic field exists, changing the z-direction magnetic field does not necessarily accelerate melting. In the series of cases with the lowest Mn_y, the addition of the z-direction magnetic field shortens the total melting time. In the series of cases with middle Mn_y, however, the addition of the z-direction magnetic field leads to a decrease in liquid fraction at the same Fo. This indicates that the z-direction magnetic field inhibits melting at this point. In the series of cases with the highest Mn_y, the inhibitory effect of the z-direction magnetic field is weaker than that in the series of cases with the lowest Mn_y. This shows that in the presence of a relatively strong magnetic field, the inhibitory effect of another magnetic field is also quite limited. From the $(\overline{Nu})$ variation diagram in Fig. 11(b), it can be seen that when the Mn is large and the magnetic field intensity is strong, the average $(\overline{Nu})$ exhibits fluctuations. The reason for these fluctuations is consistent with what was analyzed in the previous section: the stronger magnetic force causes more prominent disturbance of the nanofluid on the heating wall, which disrupts the stable convective heat transfer.

Figures 12(a) and 12(b) show the total heat storage and heat storage efficiency under different Mn_y and Mn_z parameters, respectively. From the heat storage data in Fig. 12(a), when a y-direction magnetic field exists, increasing the z-direction magnetic field causes heat storage to first increase and then decrease. This is due to the competition between the z-direction and y-direction magnetic fields. As mentioned in Section 4.1, enhanced magnetic convection increases heat storage, while weakened magnetic convection resulting from competition also improves heat storage. Thus, the combination of medium magnetic field intensities (e.g., $Mn_y = 5\times10^6$ and $Mn_z = 5\times10^6$) achieves the maximum heat storage. This parameter combination is a good choice if a phase change system needs to absorb more heat. In this parameter combination, adding a z-direction magnetic field can increase heat storage by up to 2.3%. The trend for heat storage efficiency is the opposite. Magnetic convection dominated by a single magnetic field can generate more vortices. As shown in Fig. 12(b), cases where magnetic convection is clearly dominated by one magnetic field have a shorter total melting time and higher heat storage efficiency. This indicates that multi-vortex modes can effectively improve heat storage efficiency. Since the two magnetic fields compete with each other and thereby inhibit the melting process, the heat storage efficiency of most dual-direction magnetic field cases is lower than that of the corresponding single magnetic field cases. The maximum inhibitory effect can reach 3.9%. Furthermore, the competitive relationship between the dual-directional magnetic fields can alter the inherent regulation characteristics of a single magnetic field. However, under the parameter combination of $Mn_y = 3\times10^6$, the reduction in the total melting time becomes less pronounced as the z-direction magnetic field intensity increases, despite the simultaneous decrease in the average temperature. To be specific, this regulation strategy enables a maximum reduction of 0.8% in the average temperature, coupled with a 6.1% extension of the total melting time at most. This result highlights the distinct superiority of dual-directional magnetic field regulation in scenarios requiring long-term temperature control.

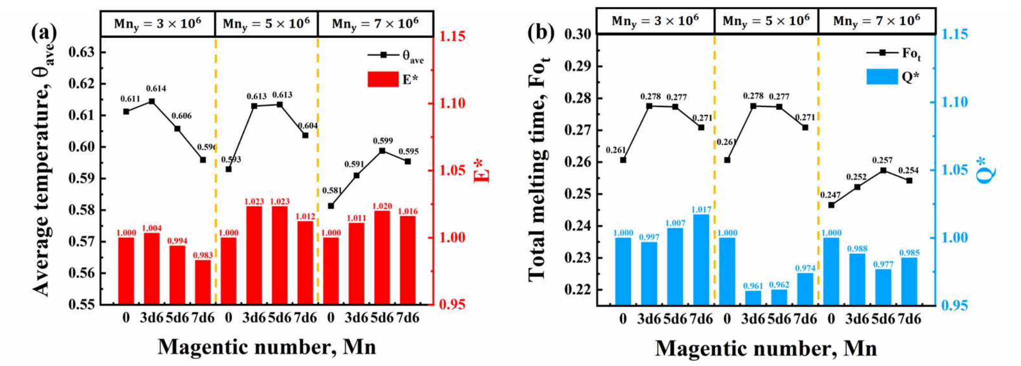

Fig. 12. (a) Variations of average temperature and total heat storage for different Mn_y and Mn_z, (b) Variations of total melting time and heat storage efficiency for different Mn_y and Mn_z.

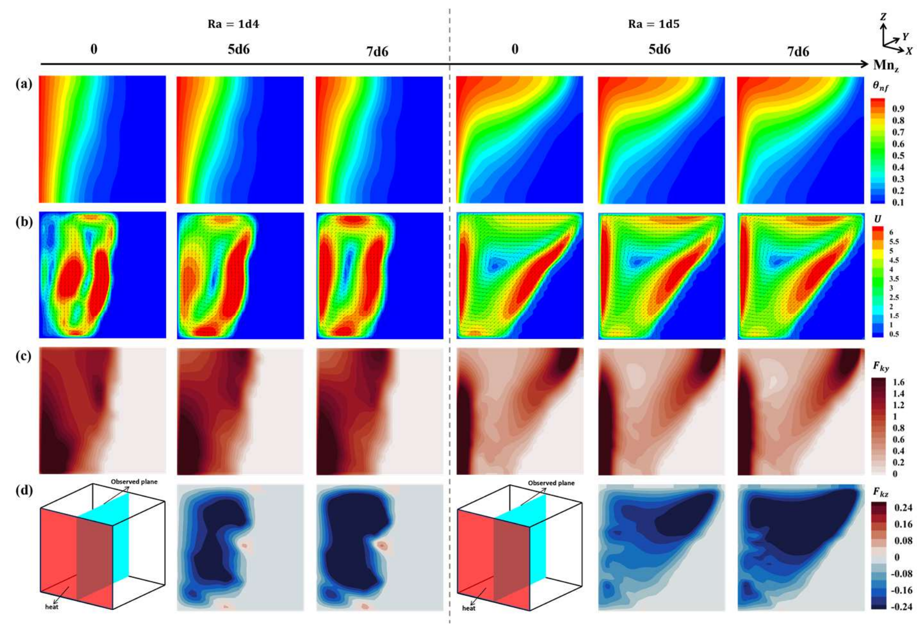

Fig. 13. Comparisons of (a) temperature field, (b) velocity field, (c) y-direction Kelvin force field and, (d) z-direction Kelvin force field distributions for Mn_z from 0 to 7×10^6 at Ra = 10^4 and 10^5.

4.3. Coupling effects of magnetic number and Rayleigh number

In the previous discussions, we found that under low Ra, the magnetic field plays an important role in the melting of NEPCMs. By changing the magnitude of the magnetic field, we can regulate the melting characteristics of NEPCMs. In this section, we will continue to discuss the impact of magnetic fields with different directions and magnitudes on the melting of NEPCMs at larger Ra.

Figure 13 shows the comparison of the coupling between the y-direction magnetic field and different z-direction magnetic fields under Ra = 1×10^4 and Ra = 1×10^5. An increase in Ra means that the intensity of natural convection also increases during the entire melting process. Figure 13(a) presents that under Ra = 1×10^4, increasing the magnetic number can promote the temperature conduction in the upper part of NEPCMs. However, under Ra = 1×10^5, the increase in magnetic number has no obvious effect on melting. This phenomenon occurs because under Ra = 1×10^4, although the intensity of natural convection is higher than that under Ra = 1×10^3, natural convection still cannot fully dominate the flow of liquid PCM. So, when the magnetic number increases, the enhanced magnetic convection can still affect the flow. When Ra rises to 1×10^5, natural convection is strong enough to dominate the flow of liquid PCM. The intensity of magnetic convection generated by the increased magnetic number is much lower than that of natural convection. Therefore, under high Ra conditions, the increase in magnetic number has no obvious effect on melting. Figure 13(b) shows that under both Ra = 1×10^4 and Ra = 1×10^5, the velocity flow mainly shows a single-vortex structure. This is also because magnetic convection is weaker than natural convection at this time, so the multi-vortex structure caused by magnetic convection before cannot be formed. From Fig. 13(c), different from the Ra = 1×10^3 condition, the y-direction Kelvin force presents a force-bridge structure as Ra increases, indicating that the Kelvin force is mainly concentrated near the heating surface and the melting front. The variation law of y-direction Kelvin force related to Ra is also consistent with previous studies [32].

Figure 14 shows the time-varying field diagrams under Ra = 1×10^4, $Mn_y = 7\times10^6$ and $Mn_z = 5\times10^6$. Figure 14(a) shows that when the intensity of natural convection is comparable to that of magnetic convection, the development of the temperature field presents a new pattern. In the middle stage of melting (Fo = 0.12), the low-temperature isotherms still maintain a certain angle with the bottom edge. This means the temperature conduction in this phase change system was relatively uniform before, with no large temperature difference between the upper and lower parts. As melting proceeds, the angle between the low-temperature isotherms and the bottom edge becomes larger and larger. This indicates that in the middle and late stages of melting, the melting rate of the upper part becomes faster and faster. In the late stage of melting (Fo = 0.20), only the lower right corner of the entire cavity is not completely melted. Figure 14(b) shows the development of the velocity field. In this case, the streamlines mainly form a single-vortex structure. In the early stage of melting, the velocity is concentrated on the heating side and the solid side. As melting proceeds, the liquid phase region becomes larger and larger. Under the influence of magnetic field regulation and natural convection, the velocity on the heating side gradually decreases, while the velocity at the bottom gradually increases. Figure 14(c) illustrates the formation and fracture process of the force-bridge in the y-direction Kelvin force field. At Fo = 0.04, when melting has just started, the y-direction Kelvin force is still uniformly distributed throughout the liquid phase region. At this point, the force-bridge has not yet formed. As melting continues, by Fo = 0.08, changes in the temperature gradient of the liquid phase region led to the formation of a force-bridge connecting the lower left to the upper right. Until melting is nearly complete (Fo = 0.20), the Kelvin force in the upper right weakens, causing the force-bridge to break. As shown in Fig. 14(d), like the y-direction Kelvin force, the shape of z-direction Kelvin force is also related to Ra. Different from low Ra, under Ra = 1×10^4 and Ra = 1×10^5, the negative region of z-direction Kelvin force almost disappears, and the positive region tends to connect into a single area covering the entire liquid phase region. At Fo = 0.04, the z-direction Kelvin force field still has positive and negative regions. Over time, the positive-region Kelvin force field gradually shrinks. At Fo = 0.12, the positive z-direction Kelvin force field disappears completely, leaving only the negative z-direction Kelvin force field in the entire liquid phase region. The absolute value of the negative z-direction Kelvin force field follows a decreasing pattern, larger in the middle and smaller at the edges.

Figures 15(a) and 15(b) show the liquid fraction variation with time and average Nu variation with time for the 6 cases discussed in this section, respectively. From Fig. 15(a), it can be seen that whether under Ra = 1×10^4 or Ra = 1×10^5, adding a z-direction magnetic field will promote the melting of NEPCMs when a y-direction magnetic field exists. In Fig. 15(b), under Ra = 1×10^4, only the average Nu of the $Mn_z = 0$ condition fluctuates. This indicates that adding z-direction magnetic field eliminates the heat transfer instability caused by the magnetic field mentioned earlier. The reason is that the competition between the z-direction and y-direction magnetic fields weakens the magnetic convection of the original magnetic field. Under Ra = 1×10^5, however, only the condition with the largest Mn_z has no fluctuation. This is because under stronger natural convection, a stronger magnetic field intensity is needed to eliminate the magnetic convection of the original magnetic field.

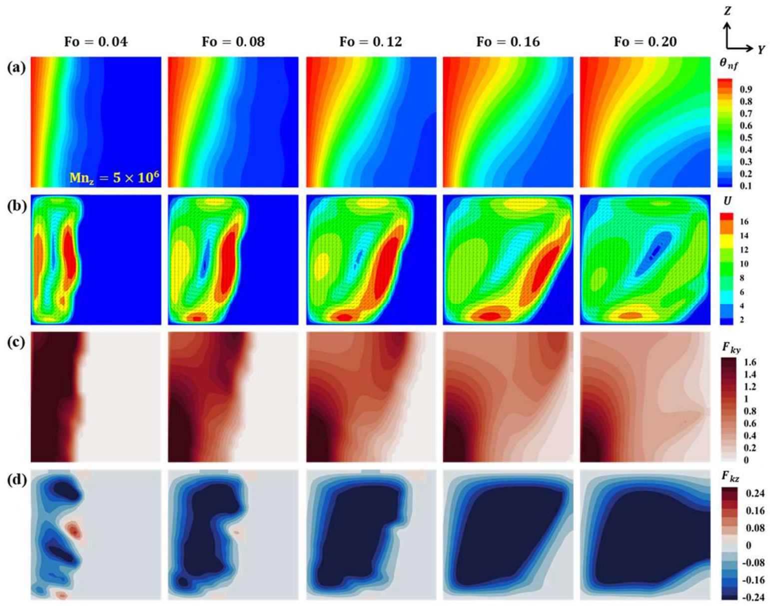

Fig. 14. Changes of (a) temperature field, (b) velocity field, (c) y-direction Kelvin force field and, (d) z-direction Kelvin force field distributions for NEPCM with Fo for $Mn_y = 7\times10^6$ and $Mn_z = 5\times10^6$ at Ra = 10^4.

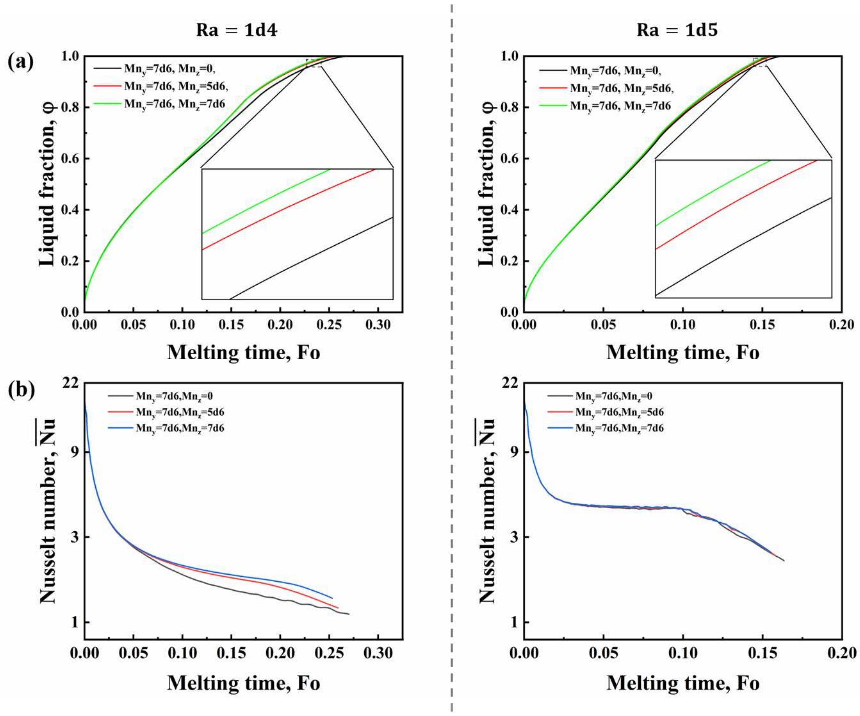

Fig. 15. (a) Variations of liquid fraction with Fo, (b) Variations of average Nusselt number with Fo for different Mn_z and Ra.

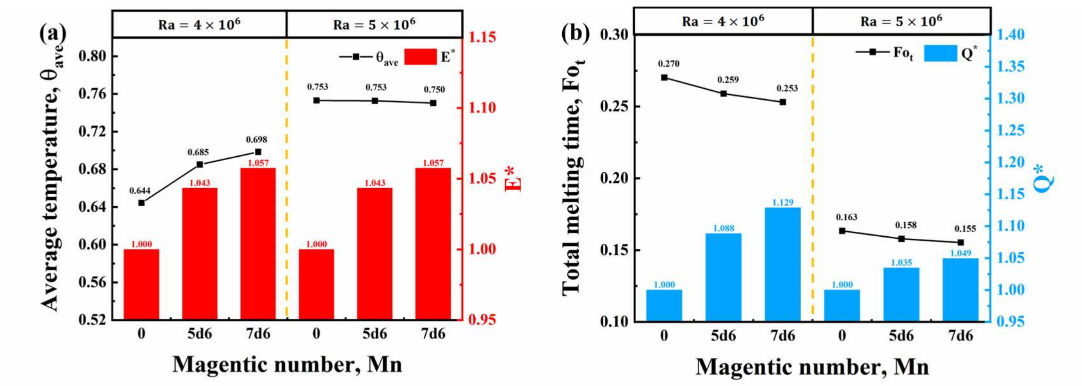

Fig. 16. (a) Variations of average temperature and total heat storage for different Ra, (b) Variations of total melting time and heat storage efficiency for different Ra.

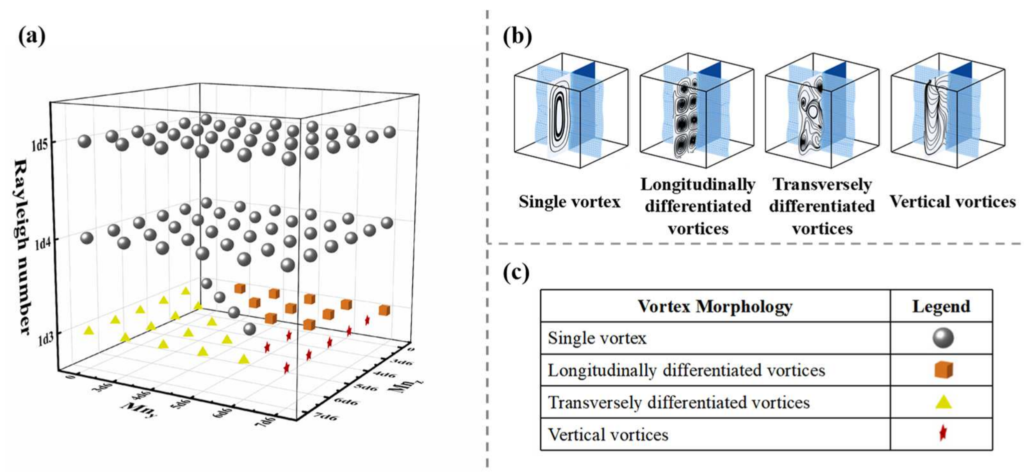

Fig. 17. (a) Formation diagram of vortex mode, (b) Schematic of vortex mode, (c) Legend for vortex mode diagram.

Figures 16(a) and 16(b) show the total heat storage and heat storage efficiency diagrams for the 6 working conditions discussed in this section, respectively. Figure 16(a) shows that after increasing Ra, changes in magnetic field intensity have almost no impact on heat storage. The maximum change in heat storage is only 0.3%. However, under Ra = 1×10^4, increasing Mn can increase the heat storage capacity of the entire NEPCM system, with a maximum increase of 5.7%. From Fig. 16(b), it can be seen that under the two groups of different Ra conditions, increasing Mn can reduce the total melting time. This indicates that the magnetic field promotes the melting of NEPCMs. The heat storage efficiency, which changes with the total melting time, also shows a trend of increasing with Mn under these two groups of different Ra conditions. Under Ra = 1×10^4, the increase in heat storage efficiency is particularly obvious, with a maximum of 12.9%. In general, under Ra = 1×10^4, adding a z-direction magnetic field to couple with the y-direction magnetic field for system regulation can improve both heat storage and heat storage efficiency. Under Ra = 1×10^5, however, adding a z-direction magnetic field to couple with the y-direction magnetic field for system regulation can improve heat storage efficiency while keeping heat storage almost unchanged.

4.4. Coupling effects of magnetic number and Rayleigh number

Figure 17 shows the schematic diagram of vortex mode formation over a range of $10^3 \le Ra \le 10^5$, $0 \le Mn_y \le 7\times10^6$, and $0 \le Mn_z \le 7\times10^6$. The blue contour in Fig. 17(b) represents the melting interface. Four vortex modes are identified: Gray sphere denotes the conventional single-vortex structure; orange cube denotes the longitudinally differentiated vortex dominated by the y-direction Kelvin force; yellow tetrahedron denotes the transversely differentiated vortex dominated by the z-direction Kelvin force; red star denotes the vertical vortex in the cavity, formed by the strong coupling of the y-direction and z-direction Kelvin forces acting on the fluid. It can be seen from Fig. 17(a) that when Ra is increased to make the natural convection induced by buoyancy stronger than magnetic convection, all vortex modes exhibit the conventional single vortex structure. At this stage, the magnetic convection caused by the Kelvin force is not strong enough to significantly disturb the fluid and form new vortices. Thus, the vortex mode remains the single-vortex structure, consistent with the non-magnetic case. Combined with the discussion in Section 4.3, since no new vortices are formed, the magnetic field regulation on melting is monotonic. In other words, increasing the magnetic field strength can monotonically improve both heat storage capacity and heat storage efficiency. At low Ra, the intensity of natural convection is weak. Magnetic convection induced by the Kelvin force more easily dominates the vortex differentiation of the fluid. At this stage, increasing either the y-direction or z-direction magnetic field can cause vortex differentiation. When the y-direction magnetic field is increased, the vortex is first longitudinally split into several regular small vortices. When the z-direction magnetic field is increased, the vortex is first transversely split before further differentiation. Multi-vortex structures dominated by either the y-direction or z-direction magnetic field all improve heat storage efficiency. This is due to their higher flow complexity compared with the single-vortex structure. When the intensities of the y-direction and z-direction magnetic fields are comparable, their competitive mechanism weakens their respective regulation effects. A conventional single vortex similar to the mutual cancellation of the two fields eventually forms. At this point, the heat storage efficiency is not significantly improved due to the competitive interaction between the two magnetic fields. When the y-direction magnetic field is sufficiently strong and the z-direction magnetic field is also present, the coupling of the two fields results in a vertical vortex structure. Although magnetic convection is strong, the number of vortices is small and thermal convection efficiency is low. Thus, the total melting time is not as good as that of other multi-vortex structures.

5. Conclusion

This study investigates the regulation mechanism of dual-directional magnetic fields on the flow, melting and thermal energy storage performance of composite phase change materials with low Fe_3O_4 concentration and high-porosity metal foam under a limited temperature difference. A verified numerical model is proposed to study the flow characteristics, melting front evolution and heat storage performance evaluation of NEPCMs. The effects of Mn_y and Mn_z in different directions and Ra on the melting process are numerically studied. The main conclusions are as follows:

- Adding a magnetic field parallel to buoyancy can effectively promote the melting of NEPCMs. The key to how this magnetic field affects NEPCM melting is that it can split the single-vortex structure generated by natural convection into a multi-vortex structure. This multi-vortex structure promotes the flow of liquid PCM, which in turn enhances heat transfer. Eventually, it speeds up the melting rate of NEPCMs. Although adding a magnetic field parallel to buoyancy can increase the heat storage efficiency of the phase change system, with a maximum increase of 4.613%, the heat storage capacity decreases as Mn increases. For the case with the highest heat storage efficiency, the heat storage capacity is also the smallest.
- The coupling between the y-direction magnetic field orthogonal to buoyancy and the z-direction magnetic field parallel to buoyancy exerts complex effects on the melting process of NEPCMs. The coupling of medium or low Mn_y and Mn_z triggers a competitive interaction between the two magnetic fields, which further destroys the magnetic convection characteristics induced by each individual magnetic field acting alone. In contrast, high intensity dual-directional magnetic fields drive the liquid NEPCMs to form vertical vortices. From the perspective of magnetic field action morphology, the force-loop structure corresponding to the y-direction Kelvin force is disrupted by the gradually intensifying z-direction magnetic field and eventually transforms into a force-column. The thermal storage capacity and thermal storage efficiency of the system depend on the strength of the competitive effect between the dual-directional magnetic fields.
- An increase in the Rayleigh number significantly weakens the effect of the magnetic field. The greater Rayleigh number enhances the dominance of natural convection, so that the magnetic convection induced by the magnetic field can no longer form a multi-vortex structure in the liquid phase change material. The morphologies of the Kelvin forces in the two directions also change accordingly: the y-direction Kelvin force transforms from the original force-loop structure into a force-bridge structure; the positive region of the z-direction Kelvin force shrinks and evolves into a sheet-like negative region that almost covers the entire liquid phase region. Since the vortex morphology is fixed as a single vortex, the introduction of the magnetic field exerts no negative effect on the heat storage capacity and heat storage efficiency. When Ra = 1×10^4, the simultaneous improvement of heat storage capacity and heat storage efficiency can be achieved. When Ra = 1×10^5, the heat storage efficiency can be enhanced without changing the heat storage capacity.

The above results reveal the regulation mechanism of the dual-directional magnetic fields and buoyancy on the melting characteristics and energy storage capacity of phase change materials, providing a theoretical basis for the optimal design of thermal management systems. In future research, we will conduct a more in-depth investigation into the coupled regulation mechanisms of complex magnetic systems, identify optimal Mn combinations for specific operating conditions and performance objectives, and explore their potential applications in thermal management and energy storage.

Author Contributions

Z. Li developed the mathematical modeling, conducted the theoretical validation, and analyzed the empirical results; Y. Zhuang undertook writing, review, editing, and supervision; designed the methodology; P. Jia performed the conceptualization, review and supervision. All authors discussed the results, reviewed the manuscript, and approved the final version.

Acknowledgments

Not applicable.

Conflict of Interest

The authors declare that there is no conflict of interest.

Funding

We would like to acknowledge the Grant support from the National Natural Science Foundation of China (52476063), Guangdong Basic and Applied Basic Research Foundation (2024A1515010845) and Shenzhen Science and Technology Programmes (GXWD20231130104619001).

Data Availability Statements

The datasets generated and/or analyzed during the current study are available from the corresponding author on reasonable request.

Nomenclature

A_{mush}	Computational morphology coefficient [kg/m^3 s]	a_{sf}	Fluid-solid interfacial surface area [m^{-1}]
c	Specific heat capacity [J/kg K]	C	Inertial coefficient
d_k	Characteristic length [m]	d_f	Fiber diameter [m]
d_p	Pore size [m]	Da	Darcy number
E	Heat storage capacity [J]	F	Liquid fraction
F	Viscosity ratio of NEPCM to pure PCM	Fo	Fourier number
F_k	Kelvin force vector [N]	G	Gravitational constant [m/s^2]
H	External magnetic field intensity vector [A/m]	h_{sf}	Interfacial heat transfer coefficient [W/m^2 K]
k	Thermal conductivity [W/m K]	k_{td}	Thermal dispersion conductivity
K	Permeability [m^2]	L	Latent heat [kJ/kg]
M	Magnetization intensity vector [A/m]	$\bar{M}$	Magnetic field parameter
Mn	Magnetic number	N	Dimensionless side length of external cubic cavity
n	Power-law index	Nu	Nusselt number
p	Pressure [N/m^2]	Pr	Prandtl Number
Q	Heat storage rate [J/s]	Ra	Rayleigh number
Re	Reynolds number	Sp	Sparrow number
Ste	Stefan number	T	Temperature [K]
T	Time [s]	u	X-velocity component [m/s]
u_m	Characteristic velocity [m/s]	U	Non-dimensional X-velocity component
U	Velocity vector [m/s]	v	Y-velocity component [m/s]
V	Non-dimensional Y-velocity component	w	Non-dimensional Y-velocity component
W	Non-dimensional Z-velocity component	x	X-coordinate [m]
X	Non-dimensional X-direction	y	Y-coordinate [m]
Y	Non-dimensional Y-direction	z	Z-coordinate [m]
Z	Non-dimensional Z-direction		

Greek symbols

α	Effective thermal diffusivity of porous medium and fluid [m^2/s]	β	Thermal expansion coefficient [K^{-1}]
ε	Porosity of copper foam	σ	Surface tension [N/m]
θ	Non-dimensional temperature	μ	Dynamic viscosity of liquid paraffin [kg/m s]
μ_0	Magnetic permeability of vacuum [T m/A]	ξ	Effective thermal diffusivity ratio between paraffin and copper foam
ξ_{cp}	Specific heat capacity ratio between paraffin and copper foam	ξ_p	Density ratio between paraffin and copper foam
Φ_{wt}	Mass fraction of nanoparticles	ρ	Density [kg/m^3]
τ_{IJ}	Non-dimensional shear stress tensor	υ	Kinematic viscosity of paraffin [m^2/s]
φ	Average liquid fraction for NEPCM	χ_m	Magnetic susceptibility
X_m	Non-dimensional magnetic susceptibility	χ_0	Reference magnetic susceptibility
χ	Tortuosity coefficient	ω	Pore density of copper foam (pores per inch, PPI)

Subscripts

eff	Effectiveness	h	Heater
nf	NEPCMs	np	Nanoparticles (Fe_3O_4)
nfe	Effectiveness of NEPCMs	p	Porous metallic matrix
s	Porous media (copper foam)	se	Effectiveness of porous media (copper foam)
∞	External environment	*	Dimensionless

References

[1] Mitali, J., Dhinakaran, S., Mohamad, A.A., Energy storage systems: a review, *Energy Storage and Saving*, 1(3), 2022, 166–216.
[2] Liu, Z., Huang, S.-M., Wang, C., Zhuang, Y., A review on non-Newtonian effects and structure-activity relationship of nanoparticles enhanced phase change materials in porous media, *Journal of Energy Storage*, 64, 2023, 107221.
[3] Chen, Y., Zhuang, Y., Feng, J.-C., Huang, S.-M., Numerical investigation on flow and heat transfer characteristics in honeycomb-like microchannel heat sink encapsulated with phase change material, *Applied Thermal Engineering*, 232, 2023, 121060.

[4] Zhuang, Y., Chen, T., Chen, J., Li, J., Guan, M., Chen, Y., Thermal uniformity performance of a hybrid battery thermal management system using phase change material and cooling plates arrayed in the manner of honeycomb, *Thermal Science and Engineering Progress*, 26, 2021, 101094.
[5] Elshaer, A.M., Soliman, A.M.A., Kassab, M., Hawwash, A.A., The effect of melting point and combination of phase change materials on the thermal control performance of small satellites in the thermal environment of low earth orbit: Numerical study, *Journal of Energy Storage*, 59, 2023, 106531.
[6] Huang, Z., Feng, J.-C., Zhuang, Y., Coupling effects, regulation mechanisms and applications of thermal-fluid-magnetic in composite phase change systems: A comprehensive review, *Journal of Energy Storage*, 118, 2025, 116200.
[7] Sáchica, D., Treviño, C., Martínez-Suástegui, L., Numerical study of magnetohydrodynamic mixed convection and entropy generation of Al2O3-water nanofluid in a channel with two facing cavities with discrete heating, *International Journal of Heat and Fluid Flow*, 86, 2020, 108713.
[8] Li, W.Q., Qu, Z.G., He, Y.L., Tao, W.Q., Experimental and numerical studies on melting phase change heat transfer in open-cell metallic foams filled with paraffin, *Applied Thermal Engineering*, 37, 2012, 1–9.
[9] Zhang, S., Feng, D., Shi, L., Wang, L., Jin, Y., Tian, L., Li, Z., Wang, G., Zhao, L., Yan, Y., A review of phase change heat transfer in shape-stabilized phase change materials (ss-PCMs) based on porous supports for thermal energy storage, *Renewable and Sustainable Energy Reviews*, 135, 2021, 110127.
[10] Han, L., Zhang, X., Ji, J., Ma, K., Research progress on the influence of nano-additives on phase change materials, *Journal of Energy Storage*, 55, 2022, 105807.
[11] Heidari, H., Mohebbi, R., Kazemi, A., Forced convection heat transfer of Ag–MgO/water micropolar hybrid nanofluid inside a stairway channel, *International Journal of Modern Physics C*, 32(11), 2021, 2150147.
[12] Zhuang, Y., Lin, J., Liu, A., Numerical investigation on non-Newtonian melting heat transfer of phase change material composited with nanoparticles and metal foam in an inner heated cubic cavity, *Journal of Energy Storage*, 51, 2022, 104417.
[13] Zhang, D., Guan, J., He, Z., Shen, C., Cao, H., Experimental investigation on heat transfer and flow patterns of pulsating heat pipe assisted by ultrasonic cavitation, *International Journal of Heat and Mass Transfer*, 183, 2022, 122187.
[14] Cui, W., Li, X., Li, X., Lu, L., Ma, T., Wang, Q., Combined effects of nanoparticles and ultrasonic field on thermal energy storage performance of phase change materials with metal foam, *Applied Energy*, 309, 2022, 118465.
[15] He, K., Zhao, Y., Wang, L., Numerical investigation on electrohydrodynamic enhancement of solid–liquid phase change in three-dimensional cavities, *International Journal of Multiphase Flow*, 168, 2023, 104562.
[16] Endigeri, H.E., Deepak Selvakumar, R., Vengadesan, S., Solid-liquid phase change subjected to unipolar charge injection from a circular wire electrode, *International Journal of Heat and Mass Transfer*, 194, 2022, 123120.
[17] Hassan, A., Cotton, J.S., An investigation of the electroconvection flow and solid extraction during melting of phase-change materials, *Journal of Electrostatics*, 128, 2024, 103904.
[18] Selvakumar, R.D., Alkaabi, A.K., Ryu, J., Lee, H., Role of dielectric force and solid extraction in electrohydrodynamic flow assisted melting, *Journal of Energy Storage*, 73, 2023, 109169.
[19] Sheikholeslami, M., Rokni, H.B., Simulation of nanofluid heat transfer in presence of magnetic field: A review, *International Journal of Heat and Mass Transfer*, 115, 2017, 1203–1233.
[20] Alkanhal, T.A., Sheikholeslami, M., Usman, M., Haq, R.-u., Shafee, A., Al-Ahmadi, A.S., Tlili, I., Thermal management of MHD nanofluid within the porous medium enclosed in a wavy shaped cavity with square obstacle in the presence of radiation heat source, *International Journal of Heat and Mass Transfer*, 139, 2019, 87–94.
[21] Çolak, E., Öztop, H.F., Ekici, Ö., MHD mixed convection in a chamfered lid-driven cavity with partial heating, *International Journal of Heat and Mass Transfer*, 156, 2020, 119901.
[22] Mehrez, Z., Maaoui, W., Najjari, M., Recent advancements in enhancing the efficiency of solar energy systems through the utilization of ferrofluids and magnetic fields, *Energy Conversion and Management*, 307, 2024, 118353.
[23] Ali, B., Hussain, S., Nie, Y., Hussein, A.K., Habib, D., Finite element investigation of Dufour and Soret impacts on MHD rotating flow of Oldroyd-B nanofluid over a stretching sheet with double diffusion Cattaneo Christov heat flux model, *Powder Technology*, 377, 2021, 439–452.
[24] Hussein, A.K., Ashorynejad, H.R., Sivasankaran, S., Kolsi, L., Shikholeslami, M., Adegun, I.K., Modeling of MHD natural convection in a square enclosure having an adiabatic square shaped body using Lattice Boltzmann Method, *Alexandria Engineering Journal*, 55(1), 2016, 203–214.
[25] Tang, R., Xu, G., Ponnore, J.J., Alqahtani, S., Anqi, A.E., Li, F., Innovative multiphysics heat transfer modeling of a non-uniform mini-channel with Fe3O4 nanofluid under a dipole magnetic field, *Results in Engineering*, 28, 2025, 107488.
[26] Li, Y., Li, N., Zhang, X., Yuan, Z., Tang, S., Wang, L., Deng, Z., Compact serpentine high head liquid metal electromagnetic pump with dual linear Halbach array, *Thermal Science and Engineering Progress*, 60, 2025, 103484.
[27] Zhuang, Y., Liu, Z., Xu, W., Effects of gradient porous metal foam on the melting performance and energy storage of composite phase change materials subjected to an internal heater: A numerical study and PIV experimental validation, *International Journal of Heat and Mass Transfer*, 183, 2022, 122081.
[28] Hu, Y., Shi, L., Zhang, Z., He, Y., Zhu, J., Magnetic regulating the phase change process of Fe3O4-paraffin wax nanocomposites in a square cavity, *Energy Conversion and Management*, 213, 2020, 112829.
[29] Li, H., Zhuang, Y., Feng, J.-C., Huang, S.-M., Experimental study on the solidification and melting performances of magnetic NEPCMs composited with optimized filling metal foam in a uniform magnetic field, *Solar Energy*, 263, 2023, 111927.
[30] Liu, Z., Zhuang, Y., Feng, J.-C., Huang, S.-M., Dynamic tuning of phase change interfacial thermal energy transport in hybrid nano-enhanced phase change materials by a non-uniform magnetic field, *International Journal of Heat and Mass Transfer*, 209, 2023, 124130.
[31] Zhuang, Y., Liu, Z., Xu, W., Experimental investigation on the non-Newtonian to Newtonian rheology transition of nanoparticles enhanced phase change material during melting, *Colloids and Surfaces A: Physicochemical and Engineering Aspects*, 629, 2021, 127432.
[32] Xu, W., Huang, T., Huang, S.-M., Zhuang, Y., Regulation mechanism of magnetic field on non-Newtonian melting and energy storage performance of metal foam composite nano-enhanced phase change materials, *International Journal of Heat and Mass Transfer*, 200, 2023, 123501.
[33] Zhuang, Y., Huang, T., Feng, J.-C., Oscillatory instability of magneto-convection during the melting of non-Newtonian ferromagnetic nano-enhanced phase change materials at low Rayleigh number, *Applied Thermal Engineering*, 248, 2024, 123306.
[34] Laouari, A., Mahfoud, B., Bessaïh, R., Hadjadj, A., Hydrodynamic instabilities in swirling flow under axial magnetic field, *European Journal of Mechanics - B/Fluids*, 85, 2021, 245–260.
[35] Dai, R., Wu, Y., Mostaghimi, J., Tang, L., Zeng, M., Characteristics and control mechanism of melting process under extra magnetic force fields, *Applied Thermal Engineering*, 167, 2020, 114704.
[36] Xu, W., Liu, Z., Huang, S.-M., Zhuang, Y., Evaluation and development of a predictive model for conjugate phase change heat transfer of energy storage system partially filled with porous media, *Energy Storage and Saving*, 1(4), 2022, 293–308.
[37] Li, W., Zhuang, Y., Wang, J., Feng, J.-C., Evolution of vortex modes and heat transfer in metal foam/nanoparticles composite phase change materials under the combined action of centrifugal force and magnetic field, *International Journal of Heat and Mass Transfer*, 255, 2026, 127860.
[38] Zhuang, Y., Huang, Z., Feng, J.-C., Non-Newtonian melting dynamics and magneto-convective modes of nano-enhanced phase change materials driven by thermocapillary convection under microgravity, *International Journal of Heat and Mass Transfer*, 236, 2025, 126284.
[39] Zheng, H., Wang, C., Liu, Q., Tian, Z., Fan, X., Thermal performance of copper foam/paraffin composite phase change material, *Energy Conversion and Management*, 157, 2018, 372–381.
[40] Ganguly, R., Sen, S., Puri, I.K., Heat transfer augmentation using a magnetic fluid under the influence of a line dipole, *Journal of Magnetism and Magnetic Materials*, 271(1), 2004, 63–73.
[41] Zhu, F., Zhang, C., Gong, X., Numerical analysis on the energy storage efficiency of phase change material embedded in finned metal foam with graded porosity, *Applied Thermal Engineering*, 123, 2017, 256–265.
[42] Nield, D.A., Bejan, A., *Convection in Porous Media*, Springer, New York, 2006.

[43] Brent, A.D., Voller, V.R., Reid, K.J., Enthalpy-Porosity Technique for Modeling Convection-Diffusion Phase Change: Application to the Melting of a Pure Metal, *Numerical Heat Transfer*, 13(3), 1988, 297–318.
[44] Tizakast, Y., Kaddiri, M., Lamsaadi, M., Double-diffusive mixed convection in rectangular cavities filled with non-Newtonian fluids, *International Journal of Mechanical Sciences*, 208, 2021, 106667.
[45] Afsana, S., Molla, M.M., Nag, P., Saha, L.K., Siddiqa, S., MHD natural convection and entropy generation of non-Newtonian ferrofluid in a wavy enclosure, *International Journal of Mechanical Sciences*, 198, 2021, 106350.
[46] Brinkman, H.C., The Viscosity of Concentrated Suspensions and Solutions, *The Journal of Chemical Physics*, 20(4), 1952, 571–571.
[47] Fourie, J.G., Plessis, J., Pressure drop modelling in cellular metallic foams, *Chemical Engineering Science*, 57(14), 2002, 2781–2759.
[48] Xu, W., Huang, Z., Zhuang, Y., Feng, J.-C., Thermocapillary convection modes and phase change heat transfer characteristics of three-dimensional metal foam composited phase change materials with different aspect ratios under microgravity, *International Journal of Heat and Mass Transfer*, 222, 2024, 125155.
[49] Boomsma, K., Poulikakos, D., On the effective thermal conductivity of a three-dimensionally structured fluid-saturated metal foam, *International Journal of Heat and Mass Transfer*, 44(4), 2001, 827–836.
[50] Kakaç, S., Pramuanjaroenkij, A., Review of convective heat transfer enhancement with nanofluids, *International Journal of Heat and Mass Transfer*, 52(13-14), 2009, 3187–3196, 3187.
[51] Georgiadis, J.G., Catton, I., Dispersion in cellular thermal convection in porous layers, *International Journal of Heat and Mass Transfer*, 31(5), 1988, 1081–1091.
[52] Žukauskas, A., Heat Transfer from Tubes in Crossflow, *Advances in Heat Transfer*, 8, 1972, 93–160.
[53] Zhuang, Y.J., Zhu, Q.Y., Numerical study on combined buoyancy–Marangoni convection heat and mass transfer of power-law nanofluids in a cubic cavity filled with a heterogeneous porous medium, *International Journal of Heat and Fluid Flow*, 71, 2018, 39–54.
[54] Madruga, S., Mischlich, G.S., Melting dynamics of a phase change material (PCM) with dispersed metallic nanoparticles using transport coefficients from empirical and mean field models, *Applied Thermal Engineering*, 124, 2017, 1123–1133.
[55] Zhang, P., Meng, Z.N., Zhu, H., Wang, Y.L., Peng, S.P., Melting heat transfer characteristics of a composite phase change material fabricated by paraffin and metal foam, *Applied Energy*, 185, 2017, 1971–1983.

ORCID iD

Zhuotao Li https://orcid.org/0009-0005-8893-2906
Yijie Zhuang https://orcid.org/0000-0002-4318-4220
Pan Jia https://orcid.org/0009-0009-5043-5313

How to cite this article: Li Z. et al., Vortex Formation Evolution in Melting of Metal-Foam-Embedded Nano-Enhanced Phase Change Materials Regulated by Dual-Directional Helmholtz Coil Magnetic Fields, *J. Appl. Comput. Mech.*, xx(x), 2026, 1–20. https://doi.org/10.22055/jacm.2026.49487.6020